

Upper Limit Tools

Ole König

ole.koenig@fau.de

Madrid, April 30, 2019

Release 1

European Space Astronomy Centre

Camino Bajo del Castillo, s/n., Urb. Villafranca del Castillo
28692 Villanueva de la Cañada
Madrid, Spain

Supervisors:

Richard Saxton (Richard.Saxton@sciops.esa.int)

Peter Kretschmar (peter.kretschmar@esa.int)

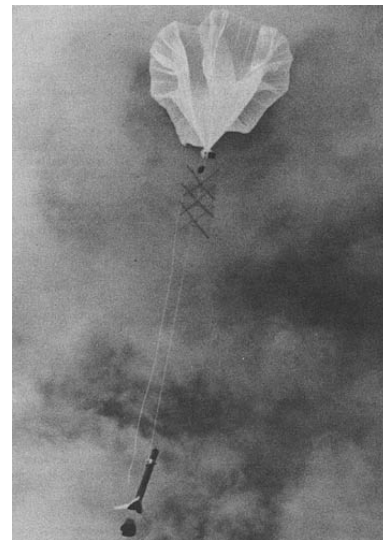
Table of Contents

1. Introduction	1
2. Upper Limit Tools	3
2.1. General description	3
2.2. The web interface	3
2.3. Catalogue calls	5
2.4. Conversion factors	5
2.5. The image database	6
2.5.1. Footprint calculations	6
2.5.2. The SQL database	7
2.6. Calculation of upper limits	7
2.6.1. Source and background counts	7
2.6.2. From counts to count rates	7
2.6.3. Upper limit calculation: Bayesian and classical statistics	8
3. Description of the missions	10
3.1. <i>Vela 5B</i>	10
3.2. <i>Uhuru</i>	10
3.3. <i>Ariel V</i>	11
3.4. <i>HEAO-1</i>	11
3.5. <i>Einstein</i> (HEAO-2)	12
3.5.1. High Resolution Imager (HRI)	12
3.5.2. Imaging Proportional Counter (IPC)	14
3.6. <i>EXOSAT</i>	17
3.6.1. <i>EXOSAT</i> LE	17
3.6.2. <i>EXOSAT</i> ME	19
3.7. <i>GINGA</i> (ASTRO-C)	19
3.8. <i>ASCA</i>	20
3.8.1. <i>ASCA</i> GIS	20
3.8.2. <i>ASCA</i> SIS	21
3.9. <i>ROSAT</i>	21
3.9.1. Position Sensitive Proportional Counter (PSPC)	23
3.9.1.1. PSPC Pointed	23
3.9.1.2. PSPC Survey	26
3.9.2. High Resolution Imager (HRI)	26
4. Scientific Application	29
5. Conclusion and Outlook	32
A. Appendix	33
A.1. Description of relevant terms	33
A.2. Further mission information	33

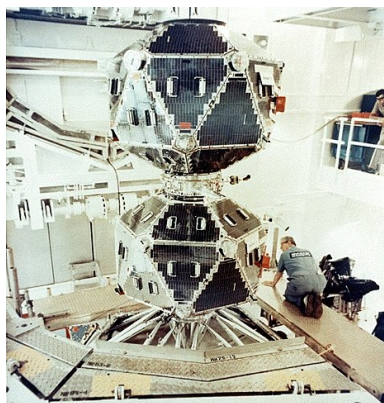
1. Introduction

A brief history of X-ray astronomy Luckily, earth's atmosphere shields earth and mankind from cosmic radiation so unlike optical astronomy, being thousands of years old, X-ray astronomy is a relatively new science. It's bound to experiments which facilitate operation in space or in the upper atmosphere. In 1929, Edward Hulbert proposed a theory on how to mount an X-ray detector on a rocket. However, it took 30 years until 1949 when the United States launched a German V2 rocket. The first and brightest celestial X-ray source was detected (Friedman, Lichtman, and Byram, 1951): The sun. In 1962, sounding rocket experiments under the lead of Riccardo Giacconi – the father of X-ray astronomy and later honored by the Nobel price – detected Scorpius X-1, the brightest extrasolar source (Giacconi et al., 1962). Two years later, Cygnus X-1 was discovered and widely accepted as first Black Hole candidate (Bleeker et al., 1967).

Scientists eventually realized that rocket experiments are impractical and would be subsequently followed first by balloons and then by satellites. In 1969, *Vela 5B*, primarily a US spy satellite for the U.D.S.S.R., detected the first gamma-ray bursts of extraterrestrial origin – the most energetic phenomena in the universe (Conner, Evans, and Belian, 1969).



A "rockoon" – a balloon with a rocket in 1956 (Corliss, 1971)



Vela 5B in the clean room (NASA)

Today's X-ray astronomy kick-started with the launch of *Uhuru* in 1970, also lead by Giacconi. The famous *Uhuru* catalogue consists of 339 sources, among it objects like supernova remnants and active galactic nuclei (Forman et al., 1978). Scientific and public interest in these highly energetic and violent objects was high and new satellites were build at an astonishing pace.

Again, one of the pushing figures was Giacconi who pursued X-ray science with the launch of *Einstein* in 1978, the first fully imaging telescope which made significant breakthrough in the field (Giacconi et al., 1979). Before, X-ray instruments used pin-hole cameras with proportional counters and had very poor spatial resolution. The introduction of grazing incidence telescope and the ability to focus resulted in the first detailed images with arcsecond resolution.

Approximately at the same time, Ken Pounds made discoveries of Active Galactic Nuclei and their relativistic wind behaviour (King and Pounds, 2003; Pounds, 2002). The German astrophysicist Joachim Trümper surprised scientists by the straight-forward measurement of the magnetic field of the neutron star Hercules X-1 (Truemper et al., 1978) – universes strongest dynamos. He lead the development of the German satellite *ROSAT* (Truemper, 1982) which monitored the entire X-ray sky, increasing the number of known sources from 840 to 125 000. In 1996 during the passage of comet Hyakutake, *ROSAT* found that also comets exhibit X-ray radiation (Lisse et al., 1996). A vast amount of other discoveries were made in the early 80s such as quasi-periodic oscillations, microquasars, relativistic jets and superluminal motion (see e.g. Mirabel and Rodríguez, 1994).

1. Introduction

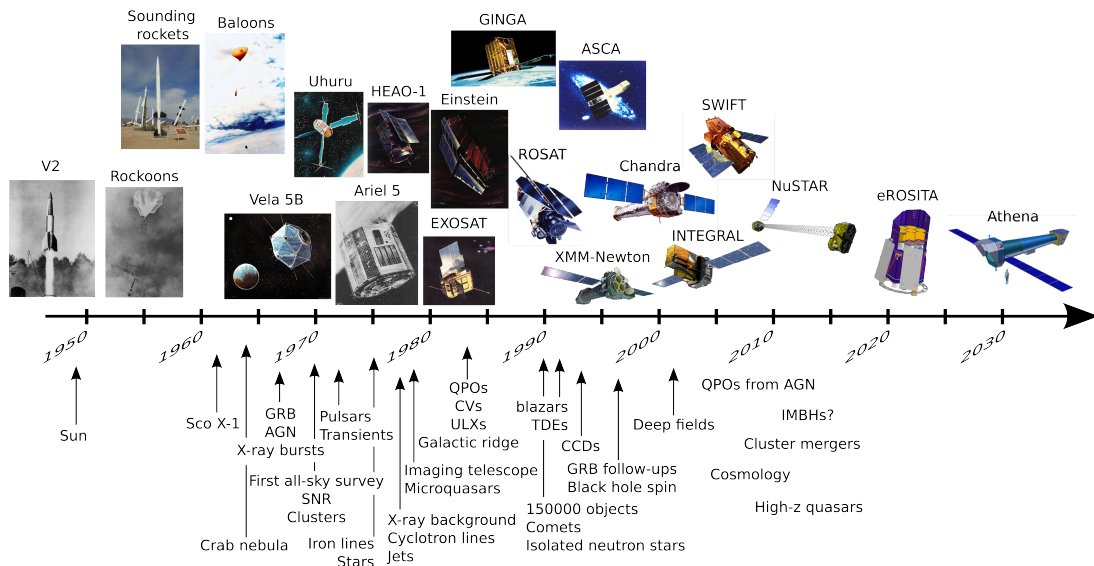
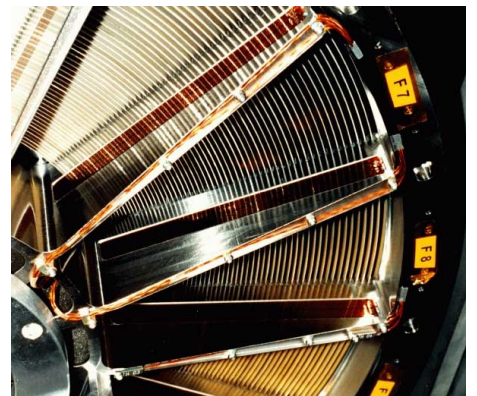


Figure 1.1.: A brief history of X-ray discoveries

Further improvement came with Japanese satellite *ASCA* which used CCD detectors, far more efficient than the old read-out procedure (Serlemitsos et al., 1995). By now the energy resolution of the instruments was good enough in order to do detailed spectroscopy and study for instance the iron lines in Active Galactic Nuclei (Duschek et al., 1980; Kormendy and Richstone, 1995).

The planets of our solar system do not emit any X-rays but reflect sun’s light. Therefore, it took a long time until they were discovered in X-rays (Bhardwaj et al., 2007). *Chandra* made fascinating discoveries of Venus (Dennerl et al., 2002) and monitored the polar aurora of Jupiter (Gladstone et al., 2002). Nowadays, leading scientists include Italian astrophysicist Luigi Piro who is known for his work on disk reflection of AGN, gamma-ray bursts and recently the discovery of electromagnetic counterparts in gravitational wave events (Troja et al., 2017).



Compared to optical light, X-ray telescopes require a completely different approach: The nested mirrors on *XMM-Newton* (NASA)

X-ray sources can be extremely variable, the flux sometimes ranges over several orders of magnitude. Some transient sources exhibit regular outbursts, others – like tidal disruption events – are highly irregular. Small scale black hole systems can be seen as down-sizing of the super-massive black holes in active galactic nuclei, reducing the timing variability from thousands of years to decades. All of this makes it exceedingly interesting to study the long-term behaviour of any X-ray source. Therefore, the interest in long lightcurves – a way to measure the variability of a source – is high. Our *upper limit tools* provide the unique opportunity to produce lightcurves at any position on the sky with a period of up to 50 years.

This document is intended as documentation about my time as trainee at the European Space Astronomy Centre in Madrid, Spain. It does not include the instruments *XMM-Newton*, *Integral*, *ROSAT* and *Swift* which were implemented by Richard Saxton.

In section 2, I describe the general operation of the *upper limit tools*, in particular the catalogue calls, footprint calculation and calculation of upper limits. Section 3 describe each mission I added, giving special attention to the footprints and catalogue calls. In section 4 I outline possible science impacts of our software. I point out further development plans and a conclusion in section 5. For a clarification of astronomical terms and abbreviations, please see section A.1 in the appendix.

2. Upper Limit Tools

The *upper limit tools* allow to generate long-term lightcurves of historical X-ray data and calculate upper limits at any celestial position via a web interface. They utilize data from 12 satellites including current observatories such as *XMM-Newton* and *Integral*, back to *ROSAT*, *EXOSAT*, *Einstein* and even *Ariel V* and *Uhuru*. This gives the genuine opportunity to calculate lightcurves for 50 years and help, e.g., researchers writing proposals.

For instance, see figure ?? for a lightcurve of 3C 273 ranging over 49 years.

2.1. General description

The *upper limit tools* enable a quick, web-based access to the data of many past X-ray missions without the hassle of browsing through several catalogues by yourself or installing software. When the astronomer clicks on the **submit** button of the *upper limit tools* website the algorithm will filter the catalogues of the available X-ray missions. This itself does not stand out to other algorithms. However, it may be the case that the detection rate was not sufficient to clearly identify a source in an image. In this case the *upper limit tools* will go to its database, search for all images which fulfill the given sky coordinates and calculate an upper limit. By adding the upper limits, the lightcurve is expanded by a tremendous number of points - especially for regions on the sky which were observed in all-sky missions, however, not detected.

This document is intended as a detailed description of the tools: The front-end with the website and the algorithms behind it calling the catalogues and calculating upper limits. Furthermore, this document describes each individual mission available and gives detailed information on e.g. the extraction of the footprints, catalogue keywords, count rate to flux conversion factors etc.

Please see also my [GitHub](#) account where I created a repository with all the relevant code I wrote during my traineeship. It also contains the PYTHON scripts – the main chunk of the software – with an extensive documentation ([here](#)). I hope that this document as well as the documentation and the repository on GitHub will make it easier for future developers to edit the project.

2.2. The web interface

On xmmuls.esac.esa.int/upperlimitserver one can find the front end of our software. The homepage consists of several panels. Under *Mission* one can activate the desired instruments for the lightcurve. The coordinates/target name or alternatively an input file with several sources can be specified in the second panel. Under *Parameters* one can choose the output energy ranges, upper limit significance, spectral model and absorption column.

Clicking on **SUBMIT** will start the software. As described above, it will browse through the catalogue and calculate upper limits at the positions where images but no catalogue entries are available. A new window (*Advanced Settings*) opens, containing the data. Clicking on  at the bottom will ask for the desired file format and download the data. Plain ASCII, CSV or a \LaTeX table is available. When clicking on  one can choose the data columns to plot. After, re-clicking the button will open a plot of the lightcurve (produced with [ZingChart](#)). This can be modified as scatter, line or spline plot and downloaded.

2. Upper Limit Tools

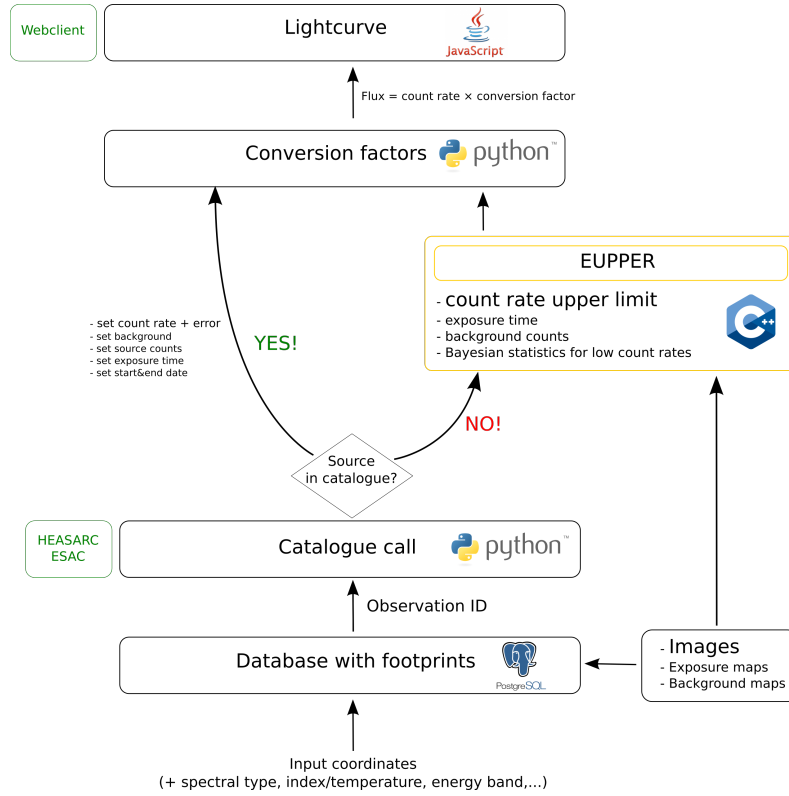


Figure 2.1.: A basic scheme of our code. The database, EUPPER and the raw images, exposure and background maps are located on the ESA servers XMMEPS (*Integral*, *ROSAT*, *ASCA*, *GINGA*, *Einstein*, *EXOSAT*, *Ariel V*, *HEAO-1*, *Uhuru*, *Vela 5B*) and XM-MXPS (*XMM-Newton*, *Swift*).

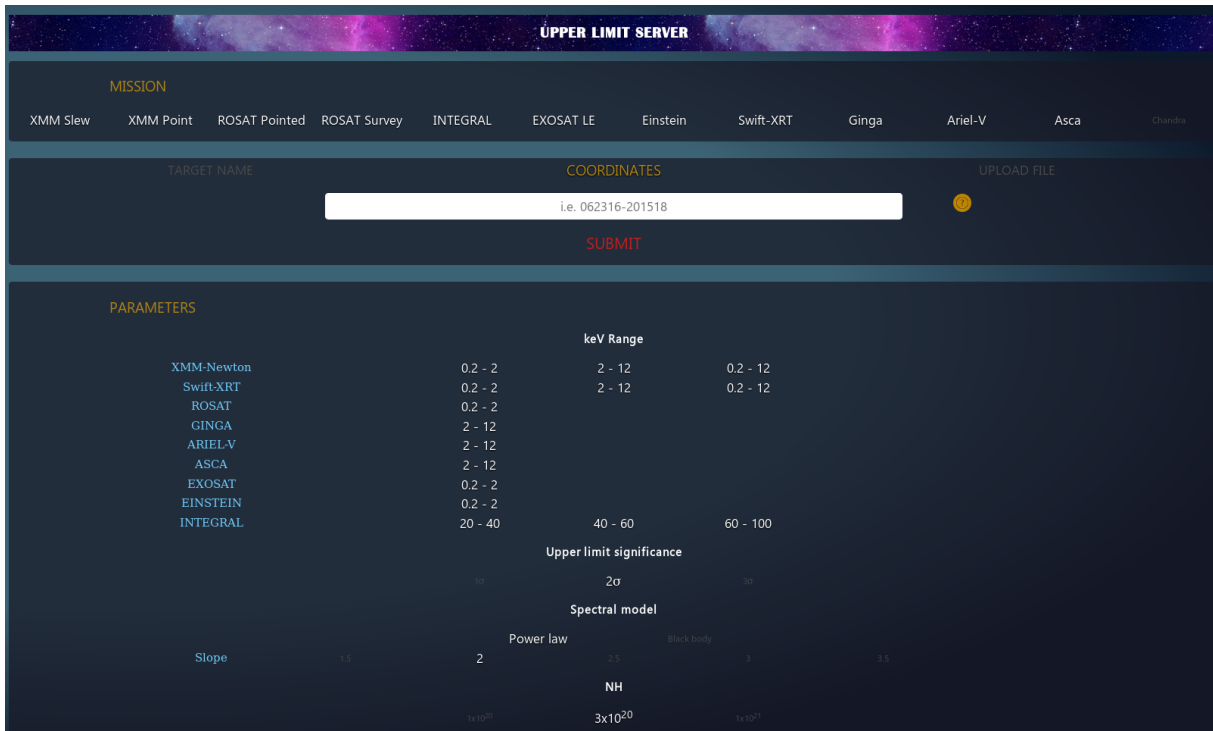


Figure 2.2.: The web interface

2.3. Catalogue calls

Due to the fact that missions as old as *Vela 5B* are included into the *upper limit tools*, catalogue calls were not always simple. Often information is missing such as background, the number of source counts, or even an exposure time or starting date. Consequently, we had to handle every catalogue by itself and pay special attention to the old catalogues. The NASA *Goddard Space Flight Center* provides the most abundant amount of catalogues and for all NASA missions we use the [W3Browse server](#) to access the data. The ESA missions such as *XMM-Newton* are accessed via a TAP call to the [NXSA server](#). Please note that our software calls the NASA and ESA servers in real-time. If their servers are malfunctioning, there will be issues with the *upper limit tools*, too.

Cone search radius In order to receive the catalogue entries we perform a cone search around the input coordinates. It is important to choose the catalogue search radius such that no sources are missed – however, also not too many sources should be identified with the same position on the sky. We orientated ourselves on the respective HEASARC *catalogue search radius*. This is an example catalogue call for the quasar 3C273 taken with the *ROSAT* HRI:

```
https://heasarc.gsfc.nasa.gov/db-perl/W3Browse/w3query.pl?tablehead=name%3dBATCHRETRIEVALCATALOG+roshri&Action=
Query&Coordinates=Equatorial+RA+Dec&Equinox=2000&Radius=1.0&Fields=Begin_Date,End_Date,Count_Rate,Count_Rate_
Error,Exposure,Box_Cts,Cir_Bkg,SeqID&Entry=187.2779,2.052&displaymode=BatchDisplay
```

Merging catalogues Several catalogues, including *XMM-Newton*, *Einstein*, and *Swift*, are divided into a data – providing the count rates, background information, etc. – and master catalogue, providing metadata such as exposure or observation time. These catalogues are linked by an observation ID or sequence number. The same observation ID also links the catalogue entries to the images. Hereby it is to be noted that one first must call the main catalogue for the source identification with the coordinates (**small** search radius) and then merge the occurring observation IDs to the image catalogue entries (bigger, arbitrary radius) and not the other way around.

2.4. Conversion factors

Unless stated otherwise, we used HEASARC’s [PIMMS](#) software to calculate the count rate to flux conversion factors. We compute every filter individually for each spectral model (powerlaw or blackbody) and spectral index/temperature. At the moment, the options are $\Gamma = 1.5, 2.0, 2.5, 3.0, 3.5$ and $k_B T = 60, 100, 300, 1000$ eV for absorption column values of $(1, 3, 10) \cdot 10^{20} \text{cm}^{-2}$ resulting in $3 \cdot 5 + 3 \cdot 4 = 27$ conversion factors for each mission (multiplied by the number of filters). We have, for instance, $3 \cdot 27 = 81$ conversion factors for the filters thin, medium and thick of *XMM-Newton* EPIC-pn. This results in thousands of conversion factors which are hard-coded into the script `convFactor.py`. They can also be found in the appendix (CREATE TABLE!).

Often you will read, that the passbands of the instrument are ”projected onto our *soft*, *hard* or *total* band”. The data of the different satellites can be only compared if they exhibit the same flux range, why we interpolate (sometimes extrapolate) the satellite-specific passbands onto our defined flux ranges:

<i>soft</i>	0.2 keV to 2.0 keV
<i>hard</i>	2.0 keV to 12.0 keV
<i>total</i>	0.2 keV to 12.0 keV

The missions *Vela 5B*, *Uhuru*, *Ariel V* and *HEAO-1* are not included in PIMMS. The literature provides conversion factors for a Crab-like spectrum ($\Gamma = 2$). However, this conversion factor

2. Upper Limit Tools

does not always match our defined *hard* band (2 keV to 12 keV). We compute the flux in *cgs* units for the two energy bands and compute the conversion factor by:

$$CF_{2-12\text{keV}} = CF_{\text{Mission band}} \cdot \frac{\text{Flux}_{2-12\text{keV}}}{\text{Flux}_{\text{Mission band}}} \quad (2.1)$$

Since we do only have a conversion factor for a powerlaw model, no matter what the input spectral model is, the output will always be a powerlaw with slope 2. We take the (small) N_H dependence into account and include – unless stated otherwise – a systematic error of $\sim 20\%$ on the conversion factors of the old missions.

2.5. The image database

2.5.1. Footprint calculations

Great effort was made to calculate the shape of the images. These so-called footprints encircle the sky region for which our code is able to compute upper limits. Often, this resembles the whole field of view of the telescope, but sometimes we constrain the region further (e.g. for *ROSAT* PSPC in sec. 3.9.1.1). The footprints are needed to find the images which match the input coordinates: If one wants to find an upper limit at a specified position on the sky the *upper limit tools* first look at all relevant catalogue entries. However, there are more images in the database than catalogue entries because often the counts are not significant enough to clearly identify a source. In this case the EUPPER code (see sec. 2.6) calculates an upper limit from the image.

To find the relevant images the footprint is used. The *upper limit tools* query the SQL database with the given R.A./Dec. coordinates and look for all images where the coordinate lies within the footprint shape. These are parsed to EUPPER.

Algorithm for footprint calculation An object-orientated PYTHON code was written by Ole König in order to calculate footprints of the illuminated region of fits images¹. There exist already sophisticated footprint finders (e.g. Stoehr, 2008), however, they turn out to have problems with low count rate images. The here-developed algorithm follows a relatively simple approach which turns out to work very well with old mission images like *Einstein* but also with newer missions like *XMM-Newton* slew. The code is publicly available and free to use. For instance, the new *XMM-Newton* slew footprints are calculated with a variation of this algorithm. The code outputs the calculated footprint as DS9 region file or SQL readable table. For old missions it transforms the FK4 1950 sky positions to FK5 J2000.

The basic steps of the algorithm are following:

1. The algorithm starts at pixel position (1,1) and walks from the edge into the image. As soon as it hits an illuminated (non-zero) pixel it puts a box (box size *b*) around the pixel and computes the average. If the value surpasses a threshold *t* the pixel is accepted as footprint point. If not, the algorithms steps further into the image until it hits the opposite border.
2. Walk the bottom x-axis to the right (with increment *i*) and repeat 1).
3. Walk the upper x-axis in the reversed direction (repeating 1)&2)) to ensure a closed shape of the footprint.
4. When all footprints are calculated it reads the RADECSYS keyword and transforms the coordinates to FK5 J2000 in case they are in FK4 1950.

¹https://github.com/olekoenig/upperlimittools/blob/master/code/additional_scripts/footprints/bigfooty.py

By increasing threshold τ the footprint points lye "deeper" in the illuminated region. This way, stray light can be excluded from the footprint. By increasing the box size \mathbf{b} the footprint shape gets "smoother". This can be useful when calculating images with very low count rates where no clear and distinct border is visible. Examples can be seen in figure 3.3.

The code assumes a relatively simple geometrical shape without holes or chips. As the algorithm walks from the edges **into** the image, it can not handle "inner structures", e.g. a donut will be reduced to a circular footprint.

2.5.2. The SQL database

We use POSTGRESQL to handle the vast amount of image metadata (mostly footprint shapes). In order to determine whether the input coordinates lye within the footprint we use **PGSPHERE**. It provides a fast search of spherical coordinates in a SQL database. We use SPOLY for the representation of polygons and SCIRCLE for cicular footprints. Our database has following entries:

- **OBSID**: The observation ID links the images to the catalogue entries: if the observation ID is available in the catalogue, the flux will be calculated from its count rate, otherwise EUPPER will calculate an upper limit from the image
- **FILENAME**: With the file name the actual image can be found to parse it to EUPPER
- **STC_S**: The footprint in FK5 J2000 right ascension and declination
- **FOV**: The polygon or circular information of the footprint in radians (for SPOLY/SCIRCLE)
- **FILT/INSTRUME**: If necessary, a filter or instrument column to apply the right conversion factors (e.g. for *Einstein*)

2.6. Calculation of upper limits

The upper limits are calculated by the code EUPPER written by Richard Saxton in C++.

2.6.1. Source and background counts

Let N be the total number of counts in the source region A_S . A_S is assumed to be radially symmetric and depends on the PSF and angular resolution of the mission. We hard-code the source radius r of each mission into our code. It typically takes a value of about 80% of the encircled energy fraction (see below). The total counts N are the sum of all counts in the source area πr^2 .

The code calculates the background counts B in background area A_B of a given ra/dec position on the sky. Ideally this is done by analyzing a background map whereby the counts of the background map in the source area ($A_B = A_S$) are summed up.

If no background map is available two circles are laid around the source and the counts within this "donut" shape are taken as the background counts.

Because we want to later compute the number of real source counts $S = N - B$ we have to ensure that the two numbers originate from the same area. Therefor, the background is normalized by multiplying with the area ratio $\frac{A_S}{A_B}$.

2.6.2. From counts to count rates

In order to calculate the background subtracted count rate we have to introduce three more concepts:

Exposure To calculate the count **rate** we will have to divide the background subtracted counts by the exposure time. If an exposure map is given the exposure is taken at the specified ra/dec position. If no exposure map is available the exposure is taken from the header of the fits image and multiplied by the vignetting factor.

Vignetting correction factor The geometry of the telescope induces a degrading illumination of the detector at the rims of the image. During the calibration of a satellite the vignetting function is computed to correct the images for this effect. The vignetting therefor reduces the effective area (and hereby the exposure time) as a function of off-axis angle. Often the vignetting factor can be assumed to be linear (see example for *Einstein* IPC in fig. 3.4).

Encircled Energy Fraction (EEF) The EEF gives the percentage of energy which is encircled in a given radius. It depends entirely on the point spread function of the instrument. We take into account that the EEF changes as a functions of source radius and off-axis angle but assume that it does not change between images of the same instrument. In other words, we hard-code the EEF values into the EUPPER code.

The background subtracted count rate [counts/s] is then computed by correcting the source counts $S = N - B$ for the EEF and dividing it by the exposure time:

$$CR = \frac{S}{\text{EEF} \cdot \text{exposure}} \quad (2.2)$$

2.6.3. Upper limit calculation: Bayesian and classical statistics

The error propagation and thus the final upper limit depends on the number of counts. Kraft, Burrows, and Nousek, 1991 showed that the application of classical Poisson-distributed statistics is unsuitable in the case of low counts. We set an arbitrary threshold of 80 counts to divide the two regimes.

Gaussian statistics For high counts above $N = 80$, we apply classical statistics and compute the error by

$$\text{Upper limit [counts/s]} = \frac{\max(S, 0) + f \cdot \sqrt{N + B}}{\text{EEF} \cdot \text{exposure}} \quad (2.3)$$

with $\sigma_S = \sqrt{N + B}$ being the error on the background subtracted counts ($S = N - B$) obtained by linear Gaussian error propagation under the assumption of a Poissonian error on N and B . The factor f can be 1,2 or 3 depending on the desired 1,2 or 3- σ confidence level (68.2%, 95.5% or 99.7%).

Bayesian statistics according to [ibid.](#) In the case of low counts we apply Bayesian statistics. Let S be again the desired number of counts which originate only from the source and B the known number of background counts (Attention: S also comes from a Poisson distribution and does not necessarily equal the **real** number of source counts). Our (posterior) probability function is given by Bayes's theorem:

$$f_{N,B}(S) = p(S) \cdot P_S(N) \quad (2.4)$$

$P_S(N)$ is called the *conditional distribution function* and is given by a Poisson-distribution for $S + B$ (for $N \rightarrow \infty$ the Poisson distribution becomes Gaussian and we can apply 2.3).

$p(S)$ is called the *prior function*. It can be shown that the posterior probability function $f_{N,B}(S)$ does not heavily depend on $p(S)$ why we can assume a uniform, positive distribution, described

2. Upper Limit Tools

by a Heaviside function. Using the knowledge that $P_S(N)$ is Poisson-distributed and evaluating the Heaviside function one obtains

$$f_{N,B}(S) = \underbrace{C}_{\text{Normalization}} \cdot \underbrace{\frac{e^{-(S+B)}(S+B)^N}{N!}}_{\text{Poisson distribution}} \quad (2.5)$$

with the normalization constant

$$C = \left[\int_0^\infty \frac{e^{-(S+B)}(S+B)^N}{N!} dS \right]^{-1} = \left(\sum_{n=0}^N \frac{e^{-B} B^n}{n!} \right)^{-1}, \quad (2.6)$$

the integral borders being shifted from $[-\infty, +\infty]$ to $[0, +\infty]$ due to the Heaviside function from $p(S)$.

The confidence interval can then be computed for a given confidence level (e.g. 95%) by

$$CL = \int_{S_{min}}^{S_{max}} f_{N,B}(S) dS \quad (2.7)$$

and the appropriate upper limit can be obtained by solving numerically for S_{max} .

Both, the count rate and the upper limit [counts/s] is then converted into flux [ergs/cm²/s] by applying the mission specific conversion factor.

3. Description of the missions

3.1. Vela 5B

General information *Vela 5B* was part of a series of US Vela satellites by the U.S. Air Force. They were primarily designed to observe whether the Soviet Union fulfills the 1963 *Partial Nuclear Test Ban Treaty*. In 1967, Vela 4 and Vela 3 discovered a flash of gamma radiation. The researchers could pinpoint the origin of the event to outer space, thereby discovering the first gamma-ray burst (Conner, Evans, and Belian, 1969).

Vela 5B flew from May 23rd 1969 until June 19th 1979 – incredible 10 years for such an old mission – and operated in spinning mode. Due to its long lifetime, *Vela 5B* enabled the unique studies of early long-term variability of X-ray binaries and transients, studied gamma-ray bursts as one of the first ever satellites and co-discovered (with ANS) X-ray bursts.

It had an energy range of 3 keV to 750 keV, however, we concentrate on the scintillation X-ray detector (XC) – an all-sky monitor. It had an energy range of 3 keV to 12 keV with 26 cm² effective area and $\sim 6.1^\circ \times 6.1^\circ$ FOV. The electric thresholds of the XC provided two energy channels: From 3 keV to 12 keV and 6 keV to 12 keV. The detector had a very high gain variation due to $\sim 60^\circ\text{C}$ temperature changes during its orbit. (HEASARC: *Vela 5B*, Whitlock, Lochner, and Rhode, 1992)

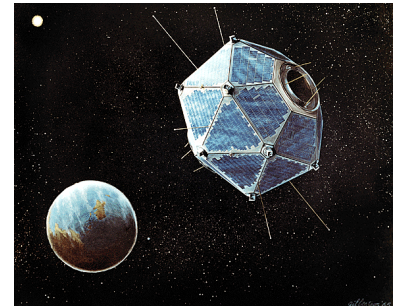
Catalogue The *VELA5B* catalogue contains data from the all-sky XC detector. We use only the 3 keV to 12 keV entries which were also corrected for the above mentioned temperature change. We use the conversion factor $(6.0 \pm 1.5) \times 10^{-12}$ ergs/cm²/s given by *ibid*. We assume a Poissonian error on the count rate. Furthermore, we set exposure time as end minus start date which is typically on the order of years. *Vela 5B* had a very high background rate of 36 counts/s which yields extremely high background counts considering the large exposure time.

We use a catalogue search radius of 6°.

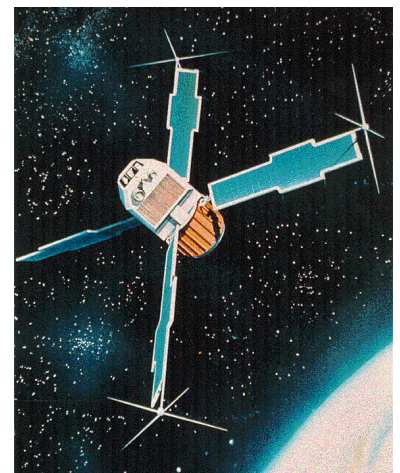
3.2. Uhuru

General information *Uhuru* – also known as Small Astronomical Satellite 1 (SAS-1) – was the first satellite entirely dedicated to X-ray astronomy. It was launched on December 12th 1970 from the San Marco platform in Kenya and flew until March 1973. The start date was the seventh anniversary of the Kenyan independence why NASA named the satellite *Uhuru*, the Swahili word for *freedom*.

Assembled were two sets of proportional counters with an energy range of 2 keV to 20 keV and an effective area of 0.084 m². The *Uhuru* mission was the first to perform a comprehensive and uniform all-sky survey with a sensitivity of 10⁻³ Crab (1.5×10^{-11} ergs/cm²/s) and scan rate of 0.5 degree/s. This resulted in the discovery of 339 X-ray sources such as binaries, supernova remnants, Seyfert galaxies and



Artist impression of *Vela 5B* (NASA)



Artist impression of *Uhuru* (NASA)

3. Description of the missions

galaxy clusters, famously dubbed the "4U sources". It also discovered the diffuse X-ray emission from galaxy clusters. The pointing capability was a few arcmin² for bright sources with a spatial resolution of $\sim 30'$. The two detectors had FOV's of $0.52^\circ \times 0.52^\circ$ and $5.2^\circ \times 5.2^\circ$, respectively. (HEASARC: Uhuru, Giacconi et al., 1971)

Catalogue The Fourth Uhuru (4U) catalogue **UHURU4** consists of 339 sources with count rate and error information which we transform to 2 keV to 6 keV flux using the conversion factor $(1.70 \pm 0.34) \times 10^{-11}$ ergs/cm²/s given by Forman et al., 1978. The conversion factor has an uncertainty of 10-20% for a Crab-like spectrum. If the count rate error field is not populated we assume a Poissonian error. Since there is no exposure, we use start date 1970-12-12 00:00:00 and end date 1973-03-18 00:00:00 with the total exposure time 71 452 800 s. We set the background to 0 and use a catalogue search radius of 1° .

3.3. Ariel V

General information After *Vela 5B* and *Uhuru*, *Ariel V* was one of the pioneers of X-ray science. From 15 October 1974 until 14 March 1980 it continuously monitored the X-ray sky and exploited new fields like long-period X-ray pulsars, bright X-ray transients containing black holes, Seyfert I galaxies and the iron line emission from extragalactic sources.

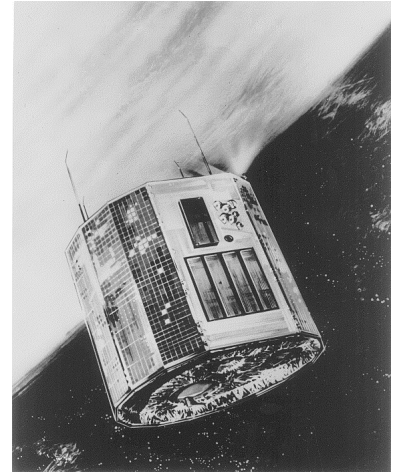
The satellite was spinning and constantly integrating the photons on its instruments over a period of $5\frac{1}{2}$ years (on the sunlit portion of the orbit). *Ariel V* had a telemetry rate of only 1 bit/s. We focus on the catalogue of the Sky Survey Instrument (SSI) which were two pairs of proportional counters (LE and HE system). One LE detector failed shortly after launch leaving an effective area of 145 cm². Every spin period (6 s) they scanned a 20×360 degree² wide band on the sky at galactic latitudes $|b| < 10^\circ$. The FOV was collimated to 0.75×10.6 degree² (FWHM) and the passband was 2 keV to 18 keV.

Catalogue The **ARIEL3A** catalogue contains 109 X-ray sources at low galactic latitude ($|b| < 10^\circ$) from the SSI instrument. We project the passband onto our *hard* band (2 keV to 10 keV). PIMMS does not include *Ariel V*, why we assume a constant count rate to flux conversion factor of $(5.3 \pm 0.8) \times 10^{-11}$ erg/cm²/s=1 SSI count/s, calculated by Warwick et al., 1981, p.880. This conversion factor assumes a Crab-like spectrum, and has an uncertainty of $\sim 15\%$.

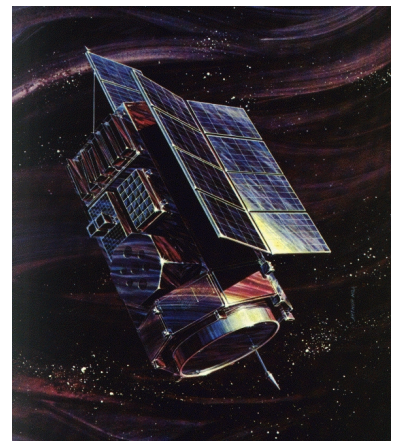
Ariel V integrated for $5\frac{1}{2}$ and since the catalogue does not provide information about start, end and exposure time, we set start time to 1974-10-18, end time to 1980-03-19 and exposure time to the difference 170 208 000 s. We use a catalogue search radius of 0.5° .

3.4. HEAO-1

General information The High Energy Astronomy Observatory was the first of a series of large NASA X-ray missions. *HEAO-1* surveyed the entire X-ray sky in the 0.2 keV to 10 MeV band for almost three times from August 12th 1977 until January 9th 1979, especially near the ecliptic poles. The payload consisted of four major instruments – A1-A4. We concentrate on the Cosmic X-ray experiment A2 which was divided into six proportional counters: two low energy detectors



Artist impression of *Ariel V* (NASA)



Artist impression of *HEAO-1* (NASA)

3. Description of the missions

(LED, 0.15 keV to 3 keV), the medium energy detector (MED, 1.5 keV to 20 keV) and three high energy detectors (HED, 2.5 keV to 60 keV). (Jahoda, Allen, and Whitlock, 1994; Rothschild et al., 1979)

Catalogue We included the Piccinotti et al. catalogue [a2pic](#) which consists of 68 extragalactic sources, including narrow emission line galaxies, broad emission line galaxies, BL Lacertae objects and clusters of galaxies. The data origins from two six month long scans and is confined to galactic latitudes $|b| > 20^\circ$, totalling 65.5% of the entire sky. PIMMS does not include the A2 mission on *HEAO-1*. Thus, we use the average conversion factor of $(2.17 \pm 0.40) \times 10^{-11}$ erg/cm²/s in the 2 keV to 10 keV, calculated by Piccinotti et al., 1982 which resembles our *hard* band. The FOV was $1.5^\circ \times 3^\circ$.

The catalogue provides two count rates from the first (Start date = 1977-08-12 00:00:00, exposure = 16 329 600 s) and second scan (Start date = 1978-03-14 00:00:00, exposure = 15 638 400 s) which we treat as two individual data points. We use a catalogue search radius of 60'.

3.5. Einstein (HEAO-2)

General Information NASA's *Einstein* satellite was the second of three "High Energy Astrophysical Observatories" and the first fully imaging X-ray telescope in space. With a resolution of only a few arcseconds and a 100x better sensitivity – unprecedented at the times – it revolutionised X-ray science. A field of view of tens of arcminutes allowed for the first time the imaging of extended objects, the detection of diffuse emission and other faint sources. The *Einstein* satellite was the first to study the spectra of supernova remnants with high spectra resolution, resolved numerous X-ray sources in the Andromeda galaxy and the Large Magellanic Clouds, studied the coronal emissions of stars and detected the X-ray jets in Cen A and M87.

Overall, *Einstein* is seen as one of the most successful X-ray missions ever. It flew from 12 November 1978 until April 1981 and had many instruments on-board where we will concentrate on the Wolter Type I telescope with the Imaging Proportional Counter (IPC, 0.1 keV to 4 keV) and the High Resolution Imager (HRI, 0.15 keV to 3.0 keV).

The user manual can be found on the [HEASARC archive](#) (D.E. Harris, 1984).

Conversion factors We use PIMMS to project the IPC and HRI passbands onto our *soft* band (0.2 keV to 2.0 keV).

3.5.1. High Resolution Imager (HRI)

The HRI was the first high-resolution X-ray camera on-board a spacecraft. It had a high spatial resolution of 3'' over the central 25' *Einstein* focal plane and even 2'' within 5' on-axis.

There are 870 High Resolution Imager FITS files produced by the Harvard CfA. The images are within a 24' FOV of the target center in the passband 0.15 keV to 3.5 keV. The background was $\sim 5 \times 10^{-3}$ cts/arcmin²/s. ([HEASARC: Einstein](#))

Catalogue Two catalogue can be found on HEASARC: [HRIIMAGE](#) and [HRIICFA](#). Neither of them include all the information we need so I merged the two catalogues by the sequence number to get the date of the observation, exposure time and count rate. The sequence number is further



HEAO-2 during flight preparation ([NASA](#))

3. Description of the missions

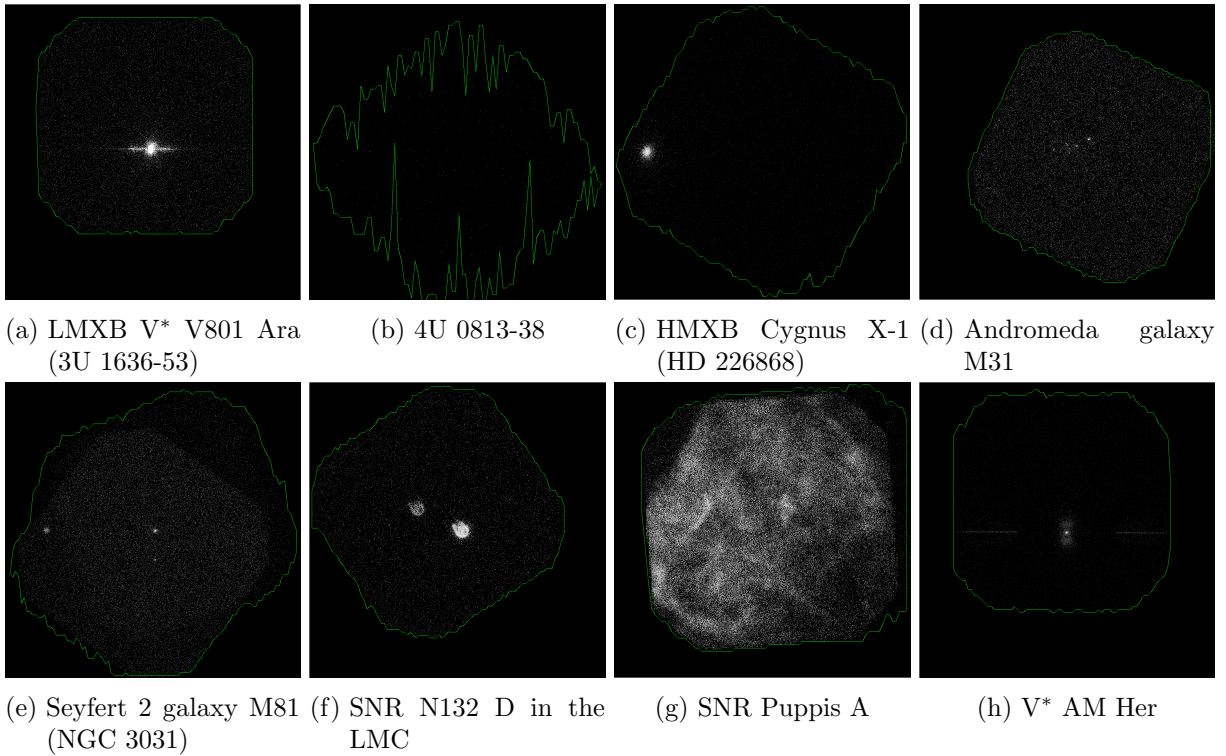


Figure 3.1.: Sample of the footprints calculated with BIGFOOTY for the *Einstein* HRI images

used as key to link the catalogue entries to the images in our database `einstein_images`. Since there is no information about the background in the catalogues, we set it to the constant value of `bkg_rate`= 5×10^{-3} cts/arcmin²/s ([HEASARC: *Einstein*](#)). The user manual (D.E. Harris, 1984, Ch.4,p.10) gives an extraction radius of 3.98'' HEW which we use for the computation of the background counts. We use catalogue search radii of 1' for HRICFA and 15' for HRIIMAGE like the HEASARC archive.

We further use the column `Net_Time` in HRIIMAGE as exposure time. `Net_Time` is the total number of seconds during which the detectors were able to gather data, corrected for Earth occultation, SAA, bad aspect solution and detector dead time. ([HEASARC: hriimage catalogue](#))

Footprint The images from the HEASARC archive have endings `.xi[a-g]`. These endings indicate how often the source was being observed. Since EUPPER requires some specific keywords, I manually appended the keywords `OBS_ID` (sequence number), `OBS_MODE` (`POINTING`), `DATE-OBS` (start of observation in fits standard), `DATE-END` (end of observation in fits standard) and renamed the file to `_xi[a-g].fits`. The footprints were calculated with my BIGFOOTY code. A sample can be seen in figure 3.1. We encounter 22 images where the fits file seems to be broken. Some images have very low count rates which results in slightly frayed footprints (e.g. fig. 3.1b).

PSF and vignetting The PSF can be approximated by ([ibid.](#), Ch.4,p.10ff)

$$PSF(r) = 2.885 \cdot 10^{-2} \cdot \exp\left(-\frac{r}{1.96''}\right) + 0.01 \cdot \exp\left(-\frac{r}{12.94''}\right) \text{ arcsec}^{-2} \quad . \quad (3.1)$$

The paper states that this is accurate for a 5' circle around the field center (on-axis) at 1.5 keV. We compute the encircle energy fraction (fig. 3.2) by integrating the PSF to the given radius and dividing it by the full PSF (integrating up to 5').

3. Description of the missions

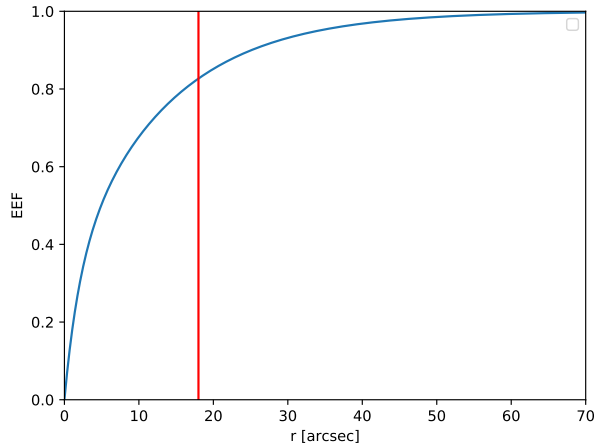


Figure 3.2.: *Einstein* HRI encircled energy fraction

We set our on-axis source radius to $18''$ which corresponds to an EEF of 0.75 (tabulated values from D.E. Harris, 1984, Ch.4,p.5) – compared to 0.83 for the empirical model. We do not take the energy dependence into account.

Currently, no vignetting correction is implemented because the user manual does not give any information.

eupper We use an $18''$ extraction radius and interpolate the EEF between 0.75 (on-axis) and 0.63 at $10'$ off-axis. (*ibid.*, Ch.4,p.5)

3.5.2. Imaging Proportional Counter (IPC)

The IPC had lower spatial ($1'$) and spectral resolution than the HRI but good efficiency and full focal plane coverage. It consisted of a Wolter Type I telescopes with a FOV of $75' \times 75' \sim 2^\circ$. Two identical detectors (except for the entrance material) were mounted on *Einstein*. The effective area was $\sim 100 \text{ cm}^2$ and the time resolution 63 ms. It had an energy range of 0.4 keV to 4.0 keV which we project onto our *soft* band. The background count rate was $\sim 1 \times 10^{-2}$ cts/s and sensitivity of 1 cts/sec / 4×10^{-11} erg/cm²/s. (*HEASARC: Einstein*, Giacconi et al., 1979, Gorenstein, Harnden, and Fabricant, 1981)

Catalogue There are two catalogues for the IPC containing 4132 fits images containing photons in the 0.2 keV to 3.5 keV range, projected onto our *soft* band: *IPCIMAGE* and *IPC*.

Neither of them include all the information we need so I merged the two catalogues. The linking was done by the sequence number in IPC and the object column in IPCIMAGE. This sequence number is then further used as key to link the catalogue entries to the images in our database *einstein_images*.

IPCIMAGE catalogue:

Here are the images of the *Einstein* IPC located. We use the entries

- **object** which is the same as the sequence number in IPC (excluding the first letter) and links the entries to the other catalogue and to the images
- **Live_Time** as exposure time, equaling the keyword TIME_LIV in our database images
- **time** as start time of the observation

IPC catalogue (Harris, 1990):

This catalogue gives the count rates of the observations. We use the entries:

3. Description of the missions

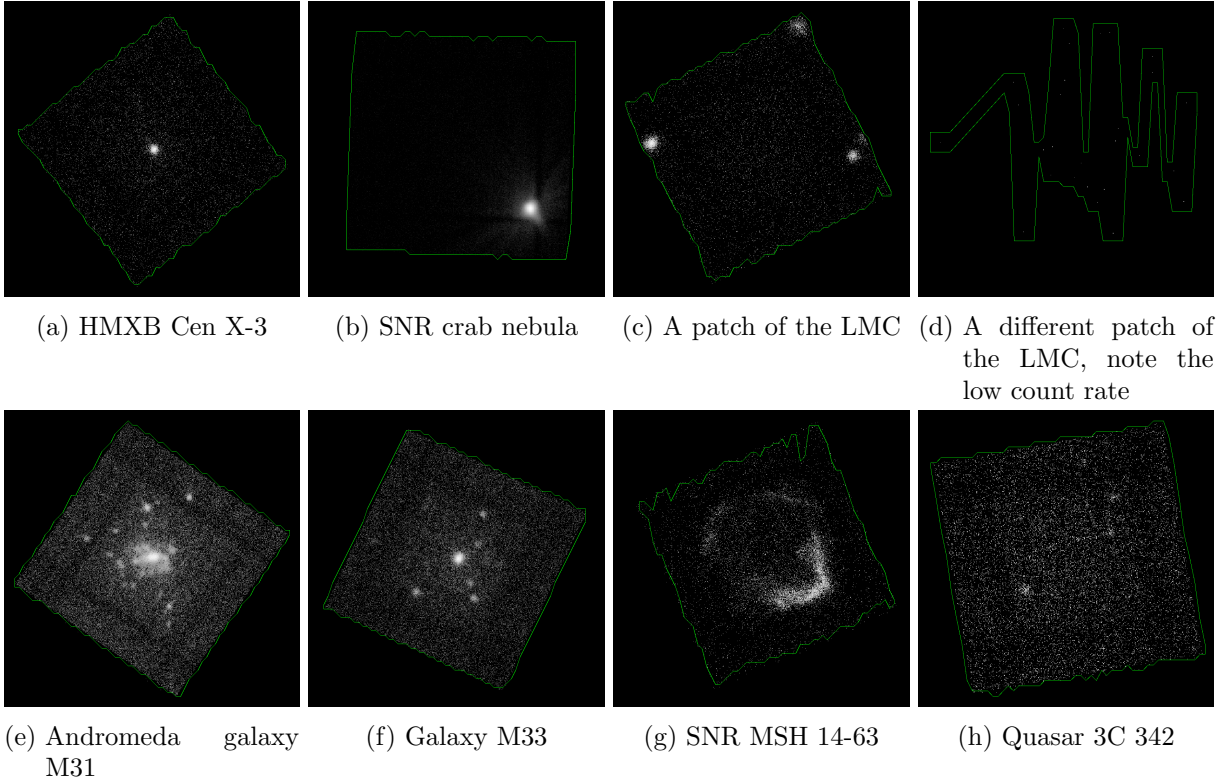


Figure 3.3.: Sample of *Einstein* IPC footprints

- **Sequence_Num:** The Einstein sequence number is a two to five digit number which uniquely identifies an Einstein observation. These numbers were assigned at the time of proposal submission
- **background_count** The total number of background counts in the detection cell of $2.4' \times 2.4'$

We use catalogue search radii of $2'$ for the IPC catalogue and $15'$ for IPCIMAGE. The FOV was 1° .

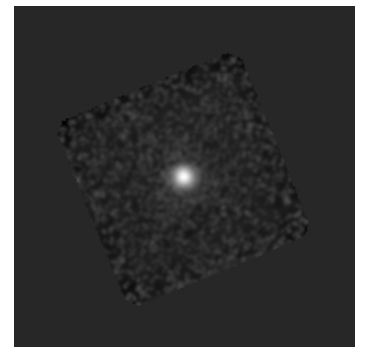
Footprints The images available on the HEASARC archive have been smoothed with a $32''\sigma$ Gaussian and were background-subtracted. This makes further processing with our code impossible since the images are in counts/arcmin² and not counts. Additionally, negative count rates emerge due to the background subtraction. To bypass this problem we used the raw event files and created images with the software **SAOImageDS9** (Beta version 8.0rc4, courtesy by Bill Joye from the Chandra X-ray Center).

Finally, I used the BIGFOOTY code to calculate the *Einstein* IPC footprints. A sample can be found in figure 3.3.

Vignetting The formula for the vignetting of the IPC is (D.E. Harris, 1984, ch.5,p.18):

$$Vign(r) = (-0.0003125 \cdot r - 0.00825) \cdot r + 0.997 \quad r [\text{arcmin}] \leq 12' \quad (3.2)$$

$$Vign(r) = 1.1049 - 0.02136 \cdot r \quad r [\text{arcmin}] > 12' \quad (3.3)$$



Einstein IPC image of 3C 273 with Gaussian smoothing (NASA W3Browse)

3. Description of the missions

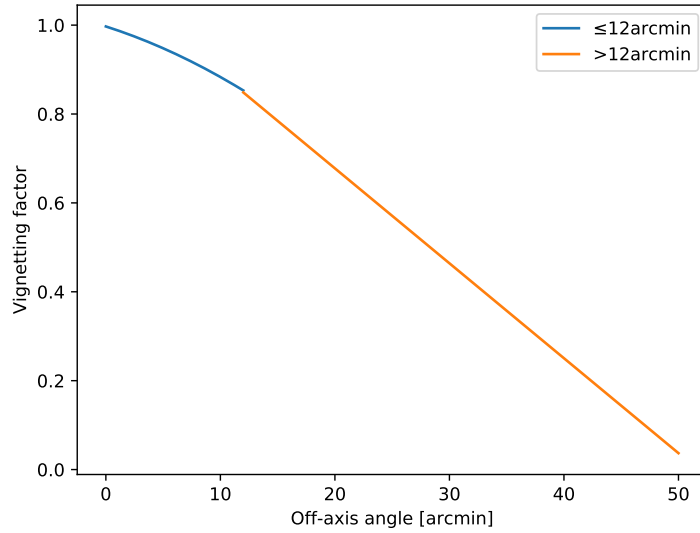


Figure 3.4.: *Einstein* IPC vignetting function

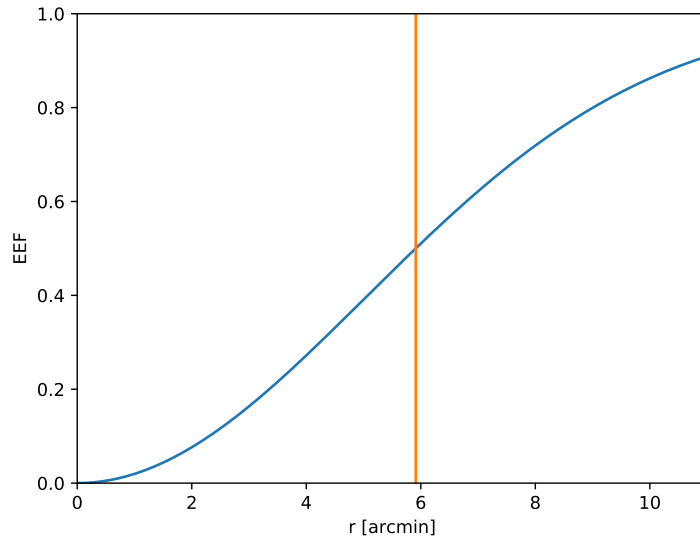


Figure 3.5.: *Einstein* IPC EEF function

Gioia et al., 1990, p.571 also states that the vignetting correction factor equals one for on-axis and increases to three for sources detected off-axis. I implemented equation 3.2 and 3.3 into the EUPPER code. The resulting vignetting function can be seen in figure 3.4.

PSF and EEF Under the assumption of a circular Gaussian response with width σ , (Harnden et al., 1984, p.24) give equation 3.4 for the fraction of total power enclosed within radius r (see fig. 3.5).

$$EEF(r) = 1 - \exp\left(-\frac{1}{2} \frac{r^2}{\sigma^2}\right) \quad (3.4)$$

We use a source radius of 5.911' which equals an EEF of 0.5.

3.6. EXOSAT

General Information ESA’s X-ray Observatory operated from May 26th 1983 to April 9th 1986. Totalling a number of 1780 observations, it contributed with scientific insight to a wide field of astronomical objects. It discovered Quasi Periodic Oscillations in LMXRB and pulsars, even over many orbital periods, helped understanding AGN variability and measured iron lines in galactic and extragalactic sources.

The payload consisted of two Wolter Type I low energy imaging telescopes (LE, 0.05 keV to 2 keV), a medium energy proportional counter (ME, 1 keV to 15 keV) and a gas scintillation proportional counter (GS, 2 keV to 20 keV). (White and Peacock, 1988, [HEASARC: EXOSAT](#))

Our main interest lies in the *EXOSAT* LE instrument since it produced 3677 images which can be analyzed by the *upper limit tools* software. We also included the *EXOSAT* ME catalogue entries. The *EXOSAT* telemetry went to the satellite dishes of the ESAC facility in Madrid, Spain.



Artists impression of *EXOSAT* (NASA)

3.6.1. EXOSAT LE

The **Low Energy** setup consisted of two identical double nested gold coated Wolter I grazing incidence telescopes with a focal length of 1.1 m. The point spread function had a size of 24" (on-axis HEW), degrading to 4' at 1° off-axis. Vignetting effects of the telescopes reduce the off-axis effective area to 45% of its peak value at 1° off-axis. In the focal plane two *channel multiplier arrays* (CMA1 and CMA2, 0.05 keV to 2.0 keV) were assembled. The CMA2 instrument failed on October 28th 1983, only 5 months into the 3 year lasting mission. Therefore, most images are detected with CMA1. (de Korte et al., 1981, [HEASARC: EXOSAT](#))

Filters The CMA detectors were also sensitive to UV radiation. Bright O and B stars could contaminate the image quality. *EXOSAT* therefore used filters to determine the degree of contamination:

From the 9 filters of the filter wheel, four were attendant to the *EXOSAT* LE images: Thick 400 nm Lexan (4Lx at FW Pos. 3), Aluminium-parylene (Al/P at FW Pos. 6), Thin 300 nm Lexan (3Lx at FW Pos. 7) and a Boron (Bor at FW Pos. 8) filter. The boron could filter the UV radiation, similar to Al/P except for the brightest and early stars. Most commonly, 3Lx, Bor and Al/P were used.

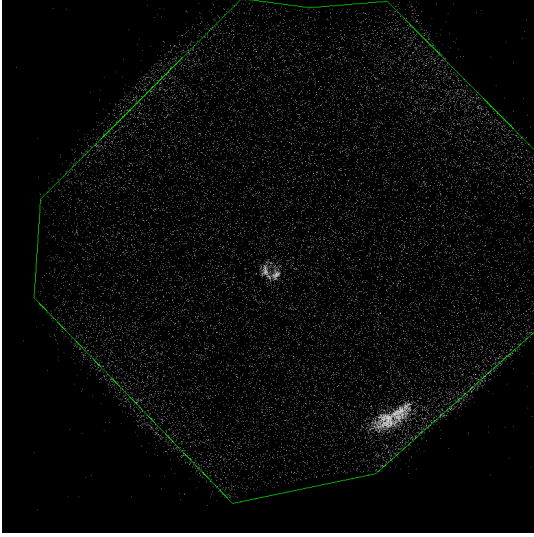
To differentiate the different filters we added a filter field to each catalogue entry in our code which links the entry to the respective conversion factor. The conversion factors project the 0.05 keV to 2 keV band onto our *soft* band of 0.2 keV to 2.0 keV.

It is possible that there are multiple observations with each filter on one day. Then, there will be several upper limits displayed.

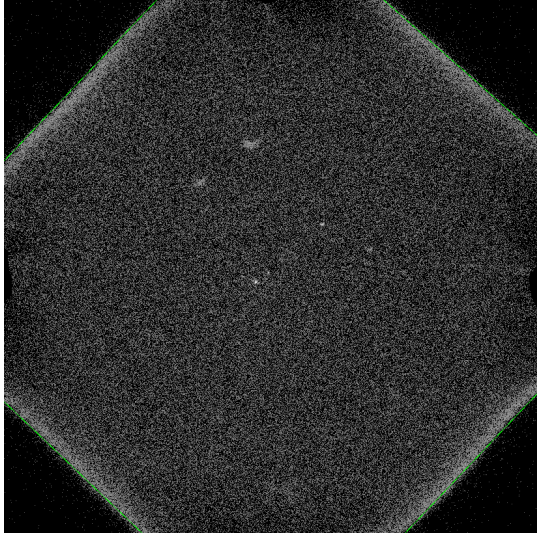
Footprints We identified four different shapes of images in the *EXOSAT* LE dataset (total of 3677 images). The images have a rectangular (~8%) or octagonal (~92%) shape, whereby the rectangular shape is smaller. Using this information, we could classify the shapes by checking the area in an 80 pixel large box (using *ftstat*) around the octagonal corner points. If the maximum value is zero we could rule out the octagonal shape.

The octagonal CMA1 and CMA2 images tend to have illuminated edges – likely due to stray light – with noise outside of the main shape. Some also exhibit extremely low count rates in the whole image. Since the pixel position of the CMA1 and CMA2 octagonal images did not change, we defined 9 (8 for CMA2, see tab. A.1 in appendix) fixed footprint points (see fig.

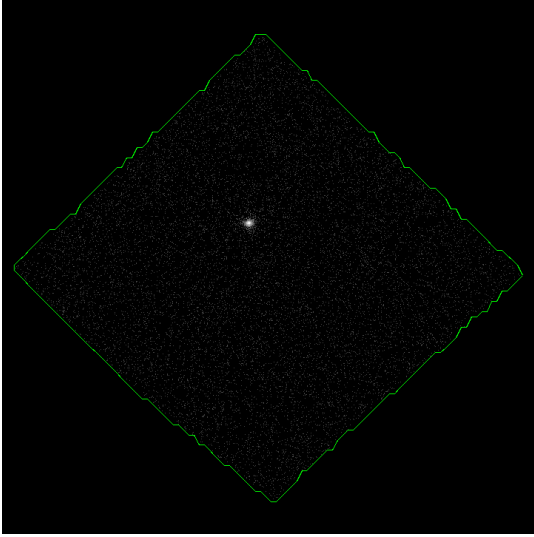
3. Description of the missions



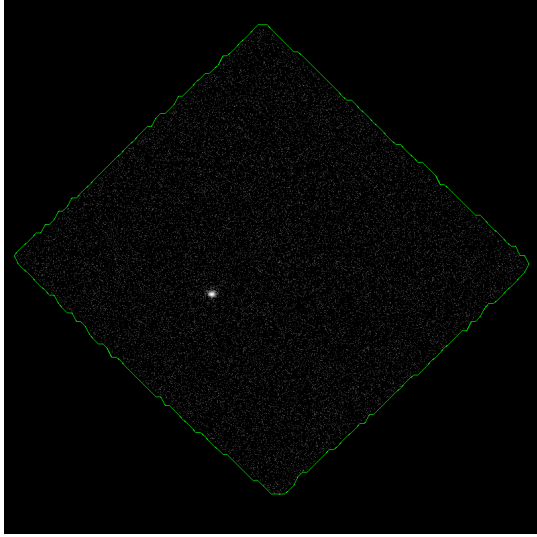
(a) CMA1 observation of the supernova remnant Cas A – this is the most abundant shape with $\sim 81\%$



(b) CMA2 observation of the HMXB Cygnus X-3 ($\sim 11\%$)



(c) CMA1 observation of the pulsar Her X-1



(d) CMA1 observation of the AM Her cataclysmic variable VV Pup

Figure 3.6.: A sample of *EXOSAT* images with the calculated footprints.

3.6a, b). The remaining rectangular images have no noise outside of the shape and we used the BIGFOOTY code to calculate the footprints (fig. 3.6c, d).

The illuminated borders, for instance in figure 3.6b, are most likely stray light effects. Furthermore, there are some images in the sample which have almost no counts. Nevertheless, these will prove important to constrain an upper limit for these coordinates.

Observation ID The observation ID is 5 letters long and determined from the ORIGFILE keyword in the fits images. It also shows up in the filename (letter 5-9) and in the catalogue as `file_image` with an additional letter in front. Removing the letter allows to generate the key in order to link the image to the respective catalogue entry.

Vignetting and encircled energy fraction

$$Vign(\text{offax}) = \begin{cases} 1 & \text{for } \text{offax} \leq 1^\circ \\ 0.45 & \text{for } \text{offax} > 1^\circ \end{cases} \quad (3.5)$$

3. Description of the missions

$$EEF(r, \text{offax}) = \begin{cases} 0.5 & r \leq 24'' \\ 0.64 & 24'' \leq r < 60'' \\ 0.2 & r \leq 24'' \\ 0.4 & 24'' \leq r < 60'' \end{cases}, \text{ for offax} \leq 6' \quad (3.6)$$

Catalogue The *EXOSAT* LE catalogue **LE** can be found on the HEASARC archive. We use a catalogue search radius of 1' for our catalogue calls like the HEASARC archive.

Background The catalogue gives additional background information [counts/s/pixel²] for the *EXOSAT* LE CMA1 detector. One pixel equals 4''. To calculate the background counts in the source region, we used an extraction radius of 24'' (on-axis half energy width of the PSF). In case we analyze the image with EUPPER (i.e. no catalogue entry at this position but position lies within the footprint of an image), we use a source radius of 1'.

3.6.2. EXOSAT ME

The **Medium Energy** instrument consisted of an array of eight proportional counters. With an energy resolution of $\frac{\Delta E}{E} = 0.2$ at 6 keV it was sufficient to detect iron lines. A FOV of 45'x45' and an effective area of $\sim 1800 \text{ cm}^2$ made it suitable for detecting sources down to 0.3 mCrab detection limit. It operated from 1.3 keV to 15 keV (Argon filled-gas cell) and 5 keV to 55 keV (Xenon filled) which we project onto our *hard* band of 2 keV to 12.0 keV. (Turner, Smith, and Zimmermann, 1981)

Catalogue *EXOSAT* ME took only lightcurves. The count rates we need for our *upper limit tools* were calculated in HEASARC's **ME** catalogue. This catalogue does not provide information about the background of the source. We therefore set it to 0. We use a catalogue search radius of 45' like the HEASARC archive. This equals the FOV.

3.7. GINGA (ASTRO-C)

GINGA ("galaxy") was the third Japanese X-ray mission and flew from February 5, 1987 - November 1, 1991. Among many others, *GINGA* discovered transients in the galactic ridge, detected cyclotron features in the X-ray pulsars 4U1538-522, V0332+53, and Cep X-4, studied the spectral evolution of transient black holes and detected the iron line emission from our galactic center region.

GINGA had a very large passband from 1 keV to 500 keV, however, we only use the Large Area Proportional Counter (LAC) in this work which had the passband 1.5 keV to 37 keV which is projected onto our *hard* band (2 keV to 12 keV). *GINGA* had a FOV of 0.8°x1.7°, an effective area of 4000 cm² and a detection limit of ~ 0.1 mCrab. (Makino and ASTRO-C Team, 1987; Turner et al., 1989)



The *GINGA* satellite (NASA)

Catalogue No images are available for *GINGA* so we only used the HEASARC catalogue **GINGALAC**. We project the 1.5 keV to 37 keV passband onto our *hard* band (2 keV to 12 keV).

GINGA is in a low-earth orbit and regularly crosses earth's radiation belts, in particular, the South Atlantic Anomaly (SAA). A further background source is the diffuse cosmic X-ray background (CXB) which is a function of sky position but not time. The background subtraction process can be found in Hayashida et al., 1989. Since the count rates of the catalogue have already been background subtracted, we set our background rate to 0.

GINGA's pointing accuracy was about $6'$, while the attitude reconstruction had an accuracy of $\sim 1'$ (**HEASARC: *GINGA***). We assume that these are 1σ values and use a catalogue search radius of $6'$. The HEASARC archive uses $60'$ but this seems to large to us.

3.8. ASCA

General information The Advanced Satellite for Cosmology and Astrophysics (*ASCA*), formerly Astro-D, took scientific measurements from February 20, 1993 - July 14, 2000 and was Japan's forth X-ray astronomy mission. It was the first satellite to use CCD detectors. NASA provided part of the scientific payload and had a guest observer program. *ASCA* was a pioneer by having imaging capability with a broad pass band, at the same time good spectral resolution and large effective area. In fact, *ASCA* was first imaging satellite covering the hard energy band above 2 keV with flux limits $\sim 1 \times 10^{-13}$ ergs/s/cm². This enabled *ASCA* to do sophisticated studies on the Fe K α line at 6-7 keV in AGN or stars. I also studied galaxy clusters and measured the heavy element abundances, consistent with type II supernova origin.



Artist impression of *ASCA* (**NASA**)

ASCA had four X-ray telescopes (XRT) composed of 120 nested gold-coated aluminum foils with a FOV of $24'$ (FWHM at 1 keV).

The resolution was $2.9'$ half power diameter. $30'$ off-center the flux reduced to 10-20%. (Arida, 1998)

Two detectors were mounted on board: a Gas Imaging Spectrometer (GIS, 0.8 keV to 12 keV) and a Solid-state Imaging Spectrometer (SIS, 0.4 keV to 12 keV).

Point spread function The PSF of *ASCA* XRT behaved in a very complex way on off-axis angle and azimuthal angle. The azimuthal dependence can be averaged. Furthermore, the GIS instrument has an additional, intrinsic PSF. The intrinsic PSF of the SIS can be neglected. (**ibid.**, XRT)

The PSF of the telescope exhibited a sharp core concentrated within $30''$ and a broad wing extended to a $3'$ (HPD). The encircled energy fraction is normalized to 1.0 at $12'$ diameter (Serlemitsos et al., 1995, fig.6a). An EEF of 0.5 is resembled at $3.3'$ and 10% flux within $30''$ (Tsusaka et al., 1995, p.4851). We use a source radius of $3.3'$ for our background calculation in EUPPER.

3.8.1. ASCA GIS

The GIS consisted of two imaging gas scintillation proportional counters with a circular FOV of $50'$ and a spatial resolution of $\sim 0.5'$ at 5.9 keV.

GIS PSF The GIS has an intrinsic on-axis Gaussian PSF with a FWHM of $0.5\sqrt{5.9\text{keV}/E}$ arcmin (Arida, 1998, XRT/fig.5.3c). Due to this additional PSF the overall spatial resolution is worse than of SIS. At $20'$ off-axis the PSF strength changes to about 85% (found by dividing the off- and on-axis peak of (**ibid.**, XRT/fig.5.3c, lower-right panel)). We are currently investigating on how to find a simple way to model the PSF.

Catalogue The *ASCA* Medium Sensitivity Survey (AMSS) is a serendipitous source survey for the extragalactic sky $|b| > 10^\circ$ and described by Ueda et al., 2001, 2005. The catalogue lists a total of 2533 5σ detected sources from an area of 278 degree² in the bands 0.7 keV to 7 keV (our *total* band), 2 keV to 10 keV (*hard*) and 0.7 keV to 2 keV (*soft*).

3. Description of the missions

ASCAGIS catalogue consists of two sub-catalogues: AMSS-I with 1343 sources between May 1993 and December 1996 and AMSS-II with 1190 sources between January 1997 and May 2000. The catalogue gives the count rate in the three bands mentioned above. We compute the count rate error following Ueda et al., (2001, p.13):

$$\sigma_{\text{CR}} = \frac{\text{CR}}{\sigma_{\text{D}}} \quad (3.7)$$

, where CR=count rate and σ_{D} the signal-to-noise ratio in units of sigma given in column SNR_Total/Hard/Soft of the HEASARC catalogue.

It does not have background information why we set this value to 0. Furthermore, it does not give exposure information why we set the exposure to the total elapsed 118 454 400 s (AMSS-I) and 99 792 000 s (AMSS-II). Note that Ueda et al., (2001, 2005) give information about start and end time, exposure time and sequence number which can be linked to the HEASARC entries by the `Field_ID`. This requires implementing table 1 of Ueda et al., (2001, 2005) which is planned in the future.

We use a catalogue search radius of 3' for the *ASCA* GIS catalogue cone search. This value is adopted from HEASARC

3.8.2. ASCA SIS

The Solid-state Imaging Spectrometer consisted of two cameras with 420x422 pixel² CCD chips, front-side illuminated. It had an energy range of 0.4 keV to 10 keV and a FOV of 22x22arcmin² with a spatial resolution of 30". (Gendreau, 1995)

PSF The intrinsic SIS point spread function is negligible. We therefore adopt the PSF value of 3.3' at an EEF of 0.5 of the XRT telescope alone.

Catalogue The **ASCASIS** catalogue is populated with target and serendipitous sources in the SIS field of view. The catalogue was published in January 1997 by Eric Gotthelf and Nicholas White, resulting from a search for point-like sources in the Public *ASCA* Data Archive. However, they point out that these are preliminary results and should be handles with care (Gotthelf and White, 1997).

No background information is given by ASCASIS why we set it to 0. The `count_rate` column in the catalogue is in the 0.5 keV to 12 keV passband which we project onto our *total* band.

We use a catalogue search radius of 5' for the *ASCA* SIS catalogue cone search.

ASCA SIS images We used the exposure maps for the calculation of the footprints with BIGFOOTY since they have cleaner borders. A sample can be found in figure 3.7.

3.9. ROSAT

General information The **RO**entgen **SAT**ellite *ROSAT* performed the first all-sky survey with an imaging telescope and a ~100x better resolution compared to *Uhuru* (*ROSAT* All-Sky Survey RASS, Truemper, 1982). The mission operated between June 1990 and February 1999 and was lead by the German Max-Planck-Institute for Extraterrestrial Physics with Guest Observer Facilities of the US and UK. Six months of the mission were dedicated to an all-sky survey and yielded the famous 2RXS catalogue, containing 135 000 sources. The X-ray telescope utilized four nested Wolter mirrors – the largest and with a roughness of <0.3 nm smoothest mirrors at the time – and operated



Artist impression of *ROSAT* (MPE)

3. Description of the missions

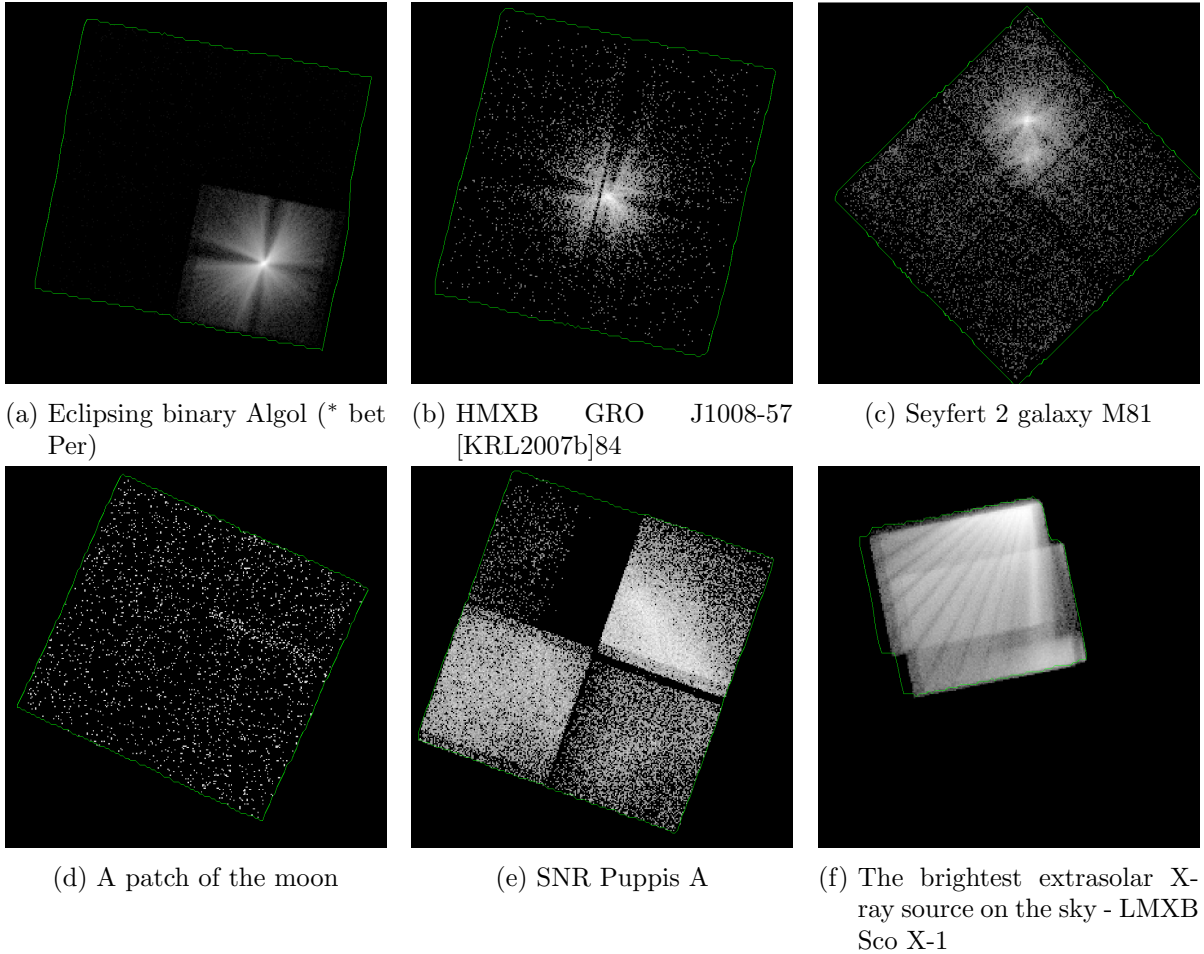


Figure 3.7.: A sample of *ASCA* SIS images with the calculated footprints

3. Description of the missions

in the soft energy band from 0.1 keV to 2.5 keV (Aschenbach, 1988).

A position sensitive proportional counter (PSPC) and an high resolution imager (HRI, 5") were located in the focal plane (Pfeffermann et al., 1987). A second telescope operated in the EUV (0.06 keV to 0.2 keV) range with the Wide-Field Camera (WFC, Pounds et al., 1993).

With the deep all-sky survey, its detection of X-rays from a comet, isolated neutron stars, shadowing by molecular clouds and morphology studies on supernova remnants, *ROSAT* made ground-breaking contributions and can be well considered as one of the most important X-ray missions ever. Due to its long operation period, large sky coverage and high exposure times, it is a very essential mission for our *upper limit tools*.

See also the <https://heasarc.gsfc.nasa.gov/docs/rosat/ruh/handbook/handbook.html> for an overview of *ROSAT*.

3.9.1. Position Sensitive Proportional Counter (PSPC)

This type of detector consists of multiwire proportional counters with modest energy ($\frac{\Delta E}{E} = 0.43 \left(\frac{E}{0.93}\right)^{-0.5}$) but high spatial resolution (25" at 1 keV) with a circular 2° diameter FOV. The effective area was 240 cm² at 1 keV and the detector operated in the full passband of the X-ray telescope (0.1 keV to 2.5 keV). Two redundant units were assembled on a carousel: PSPC-B was used for the pointed phase while detector PSPC-C was used for the survey. The wires in the detector could be suppressed with dithering of the telescope, however, the large spider features of the mirror mount remain in the images (see e.g. fig. 3.8).



The *ROSAT* PSPC detector (MPE)

3.9.1.1. PSPC Pointed

Catalogue We use the **ROSPSPC** catalogue with a search radius of 30". It contains all necessary data.

Footprints The images originate from the HEASARC archive and represent the total passband images (ending `im1`, 0.1 keV to 2.5 keV). The *ROSAT* PSPC instrument had a circular FOV. At the same time the PSF smears out a lot at large off-axis angles (see e.g. the smeared out source on the spike in 3.8b below Vela X-1) why we choose a circle of radius 0.344 125° as footprint around the center (fits keywords `RA_NOM`, `DEC_NOM`). This represents the inner circle without the spider diffraction spikes.

A sample of footprints can be seen in figure 3.8.

Exposure and background images HEASARC provides exposure maps (ending `mex`) and background images (ending `bk1`). We include the exposure maps into our EUPPER calculation. The background maps are currently not included because they are represented as 2-byte integers which are rounded to 0 by EUPPER.

Encircled Energy Fraction Instead of hard-coding specific EEF values, we implemented the radius and off-axis angle dependent encircled energy fraction according to equation 5.13 in Zimmermann et al., 1998, p.228 (eq. A.11 in the appendix). The 1 keV representation can be seen in figure 3.9.

Note that the formula is energy dependent. This energy dependence is not included in our code because the information about photon energy is irretrievably lost in the image unless one has the corresponding event lists. We therefore assume a constant energy of 1 keV. Comparing with figure 5.17 in *ibid.* this is a quite heavy approximation for zero degrees off-axis ($\sim 10 - 20\%$ uncertainty in energy range 0.5 keV to 1.7 keV, much larger at energies closer to the passband

3. Description of the missions

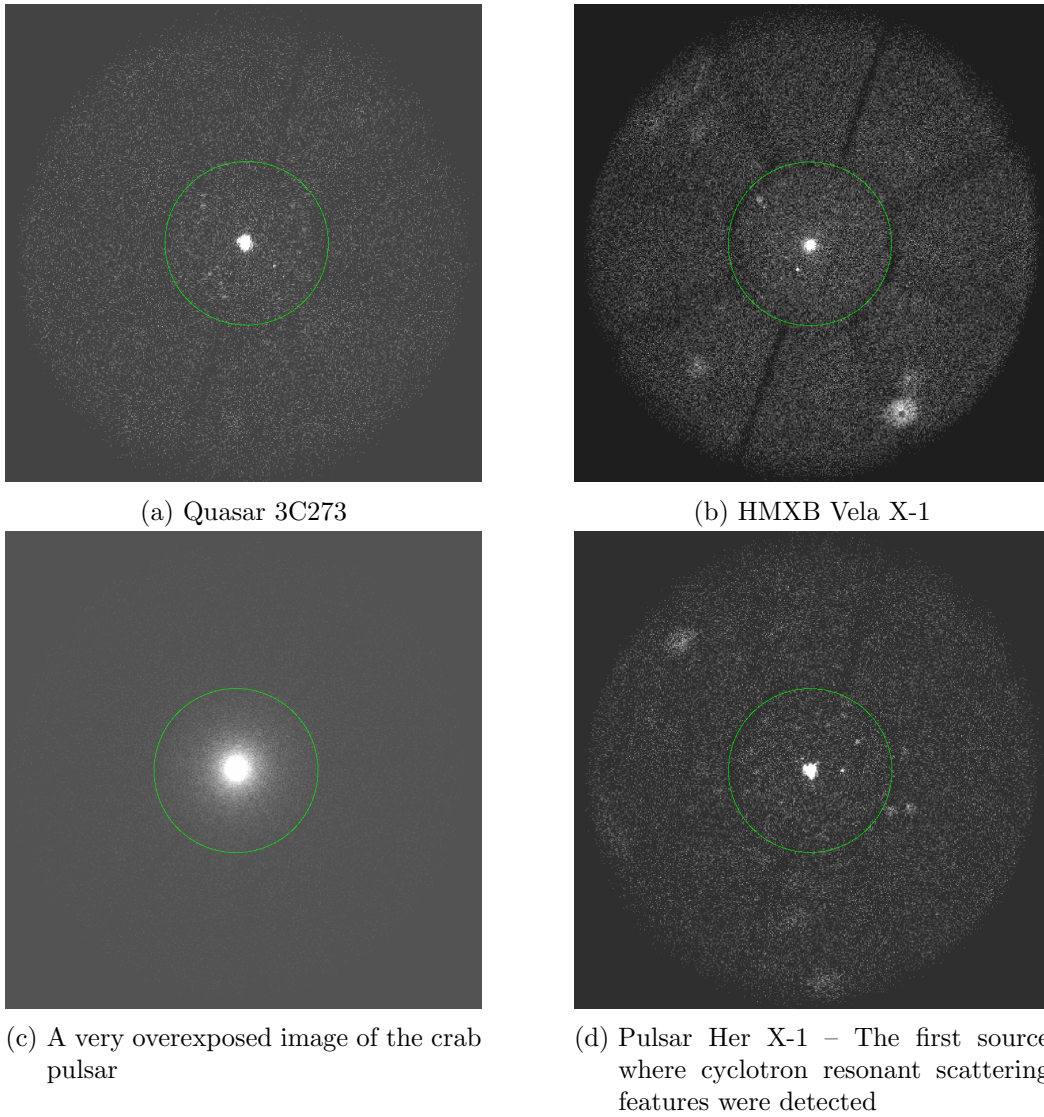


Figure 3.8.: A sample of *ROSAT* PSPC pointed images with the circular footprints

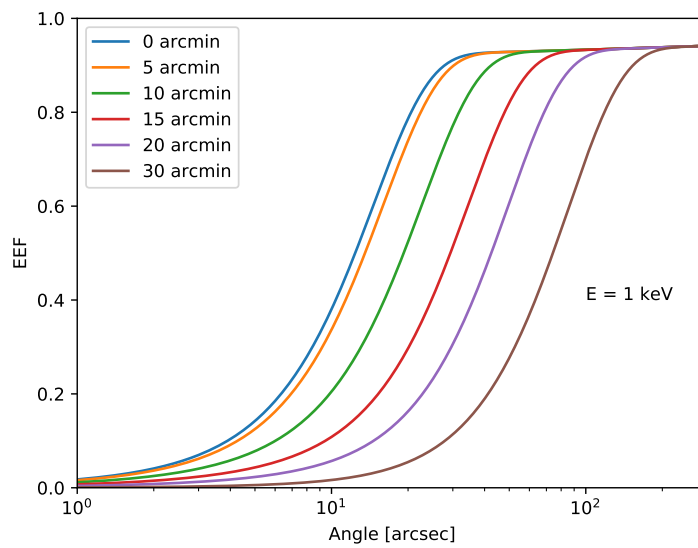


Figure 3.9.: *ROSAT* PSPC cumulative point spread function (\equiv encircled energy fraction) as a function of angle with off-axis angle dependence at energy $E = 1 \text{ keV}$ according to eq. A.11

3. Description of the missions

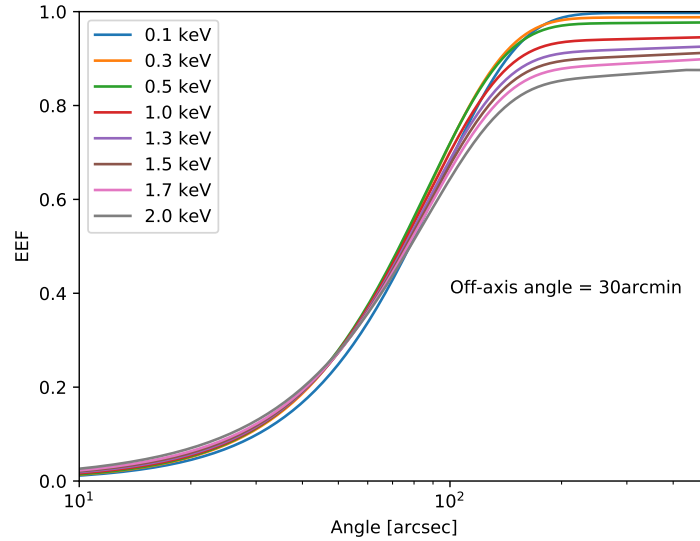


Figure 3.10.: *ROSAT* PSPC EEF as a function of off-axis angle at energy $E = 1$ keV. The variations between low and high energy are on the order of a few percent why we think that the 1 keV approximation is applicable.

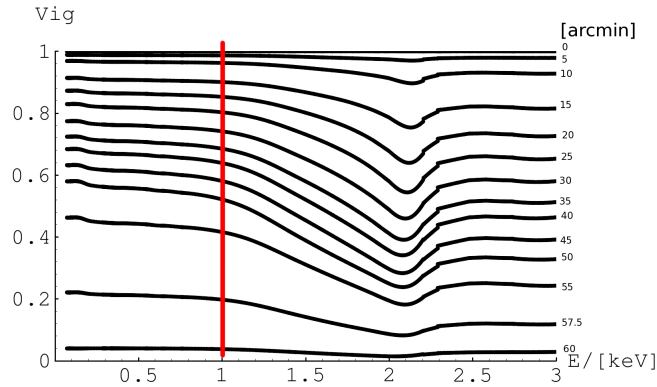


Figure 3.11.: Vignetting as a function of energy for different off-axis angles (modified from Zimmermann et al., 1998, fig 5.29)

limit) and a decent approximation for larger off-axis angles (cp. fig. 3.10: $\sim 5\%$ uncertainty in full passband 0.1 keV to 2.0 keV).

Since most images are centered on the source (on-axis) where the catalogue entries are evaluated and not the EUPPER values, we evaluate the images with EUPPER only at large off-axis angles. Therefore, we think that this approximation is acceptable (ASK RICHARD IF THIS IS A VALID CONCLUSION).

Vignetting We adopt the energy and off-axis dependent vignetting factors from Zimmermann et al., 1998, p.243, fig.5.29. Due to the reasons outlined above we take again only the 1 keV values and obtain the vignetting correction factor as cross section through the plot 3.11 (assuming a read-off error of 2%). This yields 14 points. Since our footprint radius is only $20.65'$ – i.e. we do not analyze images further away from the center then $\epsilon = 20.65'$ – we interpolate the 5 points below $20.65'$ with a linear regression to determine radius dependent values. This yields the vignetting function 3.8 as function of off-axis angle ϵ , seen in figure 3.12. The fit produces unphysical vignetting values > 1 for off-axis angles $< 1.65'$ why we set it to constant 1 (green line in 3.12).

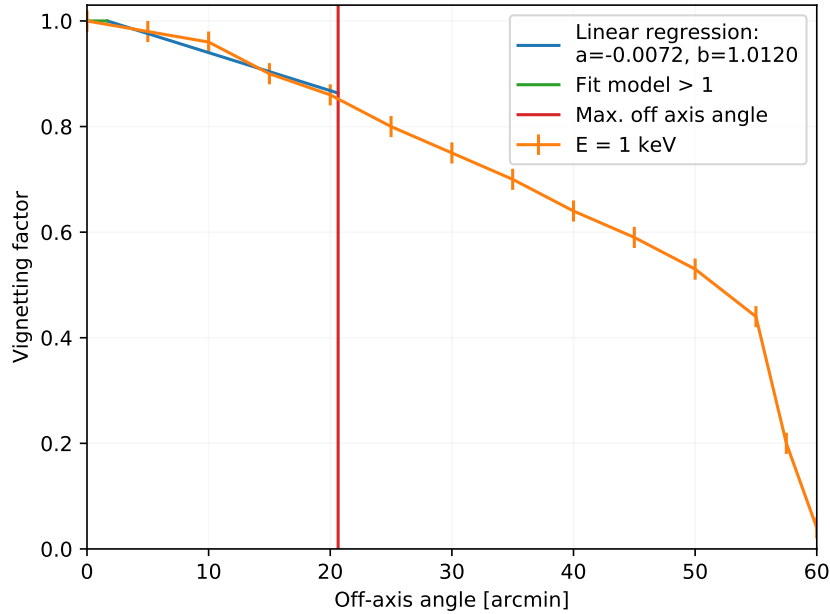


Figure 3.12.: Cross section through fig. 3.11: Vignetting as a function of off-axis angle at constant energy $E = 1$ keV

$$Vig(\epsilon) = -0.0072 \cdot \epsilon + 1.012, \quad \text{for } \epsilon < 20.6475' \quad (3.8)$$

We plan on using the tabulated values from table `vignet_pspc.tbl` as outlined in Zimmermann et al., (1998, p.246), as soon as we have access to it.

3.9.1.2. PSPC Survey

The 2RXS Catalogue The Second *ROSAT* All-Sky Survey Point Source Catalog ([RASS2RXS](#)) origins from the survey phase of the mission between June 1990 and August 1991 and contains over 135 000 sources in the 0.1 keV to 2.4 keV energy band down to a likelihood threshold of 6.5 (Boller et al., 2016). This makes it one of the most outstanding all-sky catalogue ever. We use a catalogue search radius of $2'$ to not miss any sources.

Footprints Since the survey images are rectangular we can simply adopt a rectangle with the full FOV as footprint. See figure 3.13 as example.

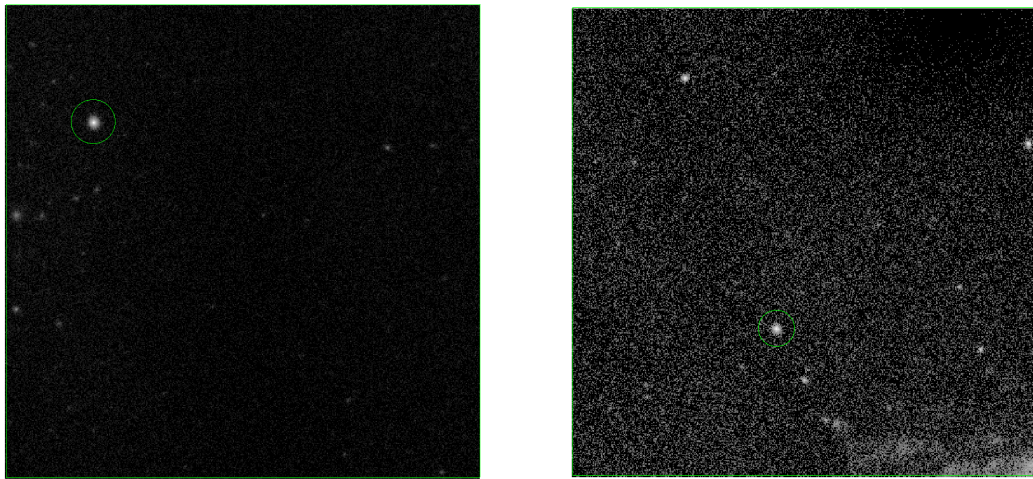
3.9.2. High Resolution Imager (HRI)

General information *ROSAT*'s high resolution imager was build up of two cascaded microchannel plates (MCPs) with a crossed grid position readout system, close to *Einstein*'s HRI. The field of view was 38×38 arcmin² with a spatial resolution of $1.7''$ (FWHM) and $61 \mu\text{s}$ temporal resolution (while suffering energy resolution).

Catalogue HEASARC's [ROSHRI](#) catalogue contains arcsecond positions and count rates for 56 401 detected sources from 5393 *ROSAT* HRI observations. In total 1.94% of the sky are covered with 13 452 high confidence detections.

The catalogue contains all necessary informations (including source and background counts). We use a search radius of $1'$ like HEASARC.

3. Description of the missions



(a) Pulsar Her X-1

(b) HMXB Vela X-1

Figure 3.13.: A sample of *ROSAT* PSPC survey images from the RASS catalogue with rectangular footprints, target is within in the circle.

Footprints From the 5373 HRI observations in the catalogue we downloaded 5347 images from HEASARC¹, ending on `_im1.fits`. The images are located in `/home/risa/richard/rosat/hri_im` on `xmmps`. We used the background images for the footprint extraction since they are smoothed and exhibit a clear, distinct border. We exclude negative background regions occurring in some images from the footprint. A sample can be seen in figure (REF). The data set exhibits 245 images with no counts – and therefore no reasonable use for us – which we reject for our database. In total our database covers 5102 footprints.

Encircled Energy Fraction The encircled energy fraction is given in Zimmermann et al., (1998, eq.(5.19)) and can be seen in figure 3.14. We use a source radius of $30''$ for our EUPPER calculation. This resembles an encircled energy fraction of 94%. As for *ROSAT* PSPC we fix the energy to 1 keV (write about this approximation)

Background maps *ROSAT* HRI background maps are located in `/home/risa/richard/rosat/hri_bk` on `xmmps`.

We include the background maps after changing the `CTYPE2` keyword from `DEC---TAN` to the fits standard `DEC--TAN`.

Exposure maps There are no *ROSAT* HRI exposure maps available on HEASARC. Therefore, the exposure is read off the `EXPOSURE` keyword.

Vignetting We plan on implementing the vignetting correction factor from table `vignet_hri.tbl` (see *ibid.*, p.246).

¹ftp://heasarc.gsfc.nasa.gov/FTP/rosat/data/hri/processed_data/

3. Description of the missions

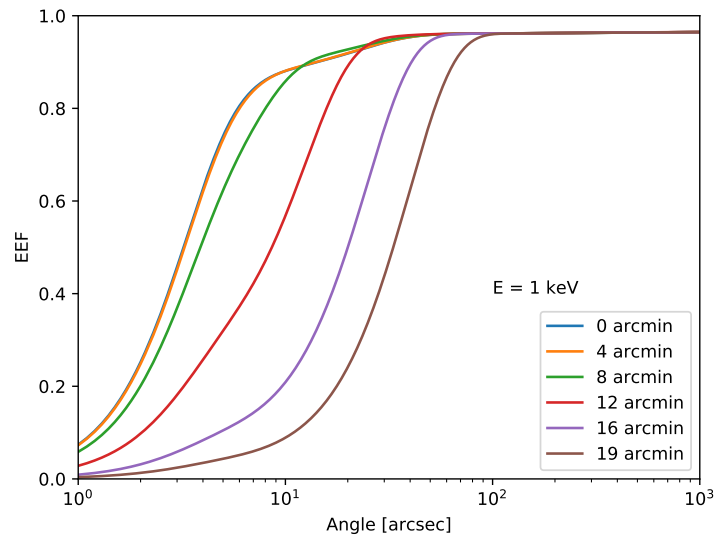


Figure 3.14.: *ROSAT* HRI cumulative point spread function (\equiv encircled energy fraction) as a function of angle with off-axis angle dependence at energy $E = 1$ keV according to Zimmermann et al., (1998, eq.(5.19))

4. Scientific Application

The scientific applications of the *upper limit tools* are manifold. First of all, lightcurves of this length are not widely available and the ability to look at any position on the sky and browse through almost all existing X-ray missions is quite unique. Many X-ray sources like AGN have timing variabilities of tens of years and studying the long-term lightcurves is essential in these cases.

Figure 4.1 shows an example lightcurve of the brightest quasar on the sky: 3C 273. This source is widely used as calibration source and known to be relatively constant over time. Even in this case the lightcurve shows a small increase in flux between year 1990 and 1997. These trends are exactly the powerful applications of the *upper limit tools*.

Transient sources like Hercules X-1 show a very different outburst behaviour. A major advantage of the length of the lightcurves is, that long-term variability cycles can be much better predicted. Finally, in figure 4.3 one sees the lightcurve of the AGN NGC 3599. So far, I showed lightcurves which had mostly catalogue entries. This lightcurves shows the power of upper limits, where the *ROSAT* upper limit constrains the flux to low values right before the big outburst.

4. Scientific Application

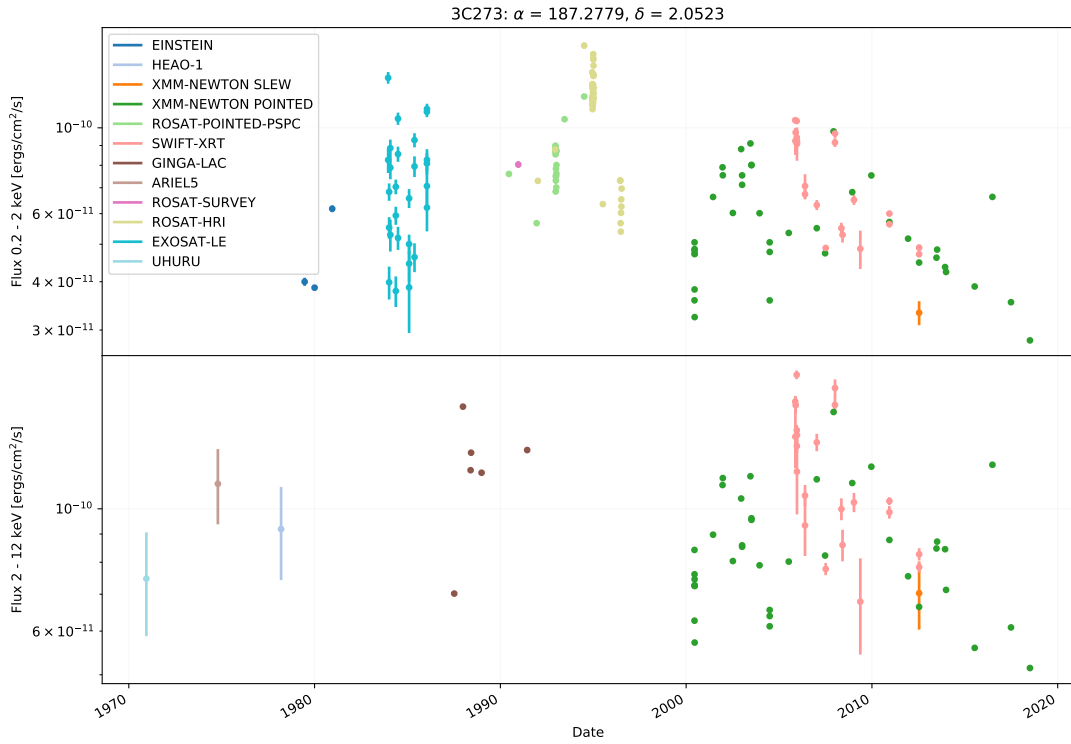


Figure 4.1.: Lightcurve of the quasar 3C 273 ranging over 46 years. This source is known for being very stable but even here, one sees small trends in the lightcurve.

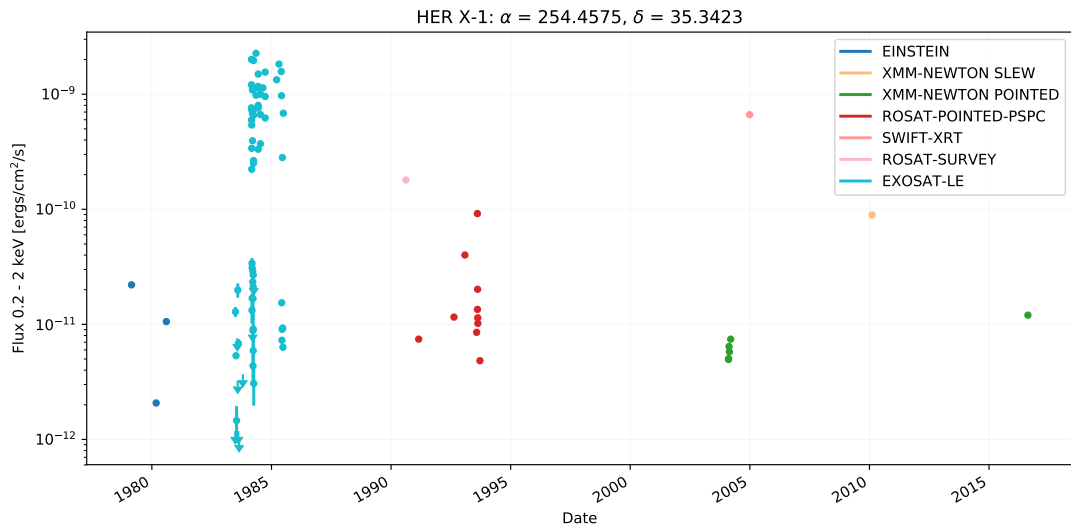


Figure 4.2.: Lightcurve of the LMXB Hercules X-1. Not the strong outburst behaviour.

4. Scientific Application

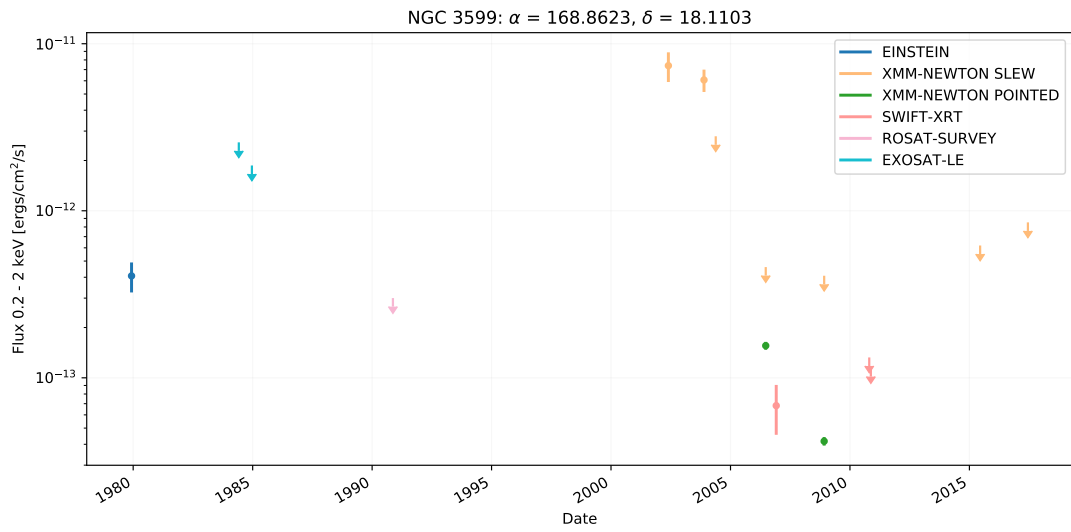


Figure 4.3.: Lightcurve of the AGN NGC 3599. Note that the *ROSAT* upper limit constrains the flux before the big outburst. The strong outburst may be due to a tidal disruption event.

5. Conclusion and Outlook

In the future we plan on including the satellites *Chandra*, *NuSTAR* and *BeppoSAX*. The all-sky telescope *eROSITA*– scheduled for launch in June 2019 – will contribute with a tremendous amount of further data points.

Please see also the project [GitHub](#)¹ page which contains the source code, documentation and useful script to plot lightcurves or calculate footprints.

¹<https://github.com/olekoenig/upperlimittools>

A. Appendix

A.1. Description of relevant terms

- Lightcurve: A lightcurve is a measure of the variability of a source. It plots flux over time. We usually plot the flux density in *cgs* units $\text{ergs}/\text{cm}^2/\text{s}$. Lightcurves are usually background subtracted where the background consists of detector noise, straylight and cosmic radiation. Constant sources will have a constant line as lightcurves. A typical lightcurve of a variable source exhibits fast-rising outbursts.
- World coordinates: We use the equatorial coordinate system with right ascension/declination (ra/dec) in degrees.

$$\alpha \text{ [decimal degrees]} = \text{Hours} \times 15 + \text{minutes}/4 + \text{seconds}/240 \text{ (1 hour} = 15 \text{ degrees)}$$

$$\delta \text{ [decimal degrees]} = \text{Deg} + \text{Arcmin}/60 + \text{Arcsec}/3600$$

- Point Spread Function (PSF): Point sources will never be displayed as exact points in an image. The point spread function describes this response of the detector to a point like source. Often this function is radially symmetric and of Gaussian shape. The resulting image is a convolution of PSF and image and an Airy disk for Gaussian PSF. Essentially, the PSF gives the probability of detecting a photon as a function of the distance from its original position on the sky. The PSF gives the flux density at every location. The differential of the PSF is the encircled energy fraction, which gives the flux within a circle of given radius.
- Half-Power diameter (HPD): The diameter within half of the focused X-rays are enclosed. Essentially a different word for full width half maximum (FWHM). Sometimes also called half energy width (HEW).
- Difference between on-axis and off-axis radius:
- Field of View (FOV): An area usually expressed in square degrees which defines the area on the sky from where the telescope receives light.
- Confidence limit and confidence interval

A.2. Further mission information

Shape	Pixel position of the footprint (x/y)					Percentage
Octagonal CMA1 3.6a	124/902	149/1278	921/2048	1181/2013	1479/2037	81.1%
	2048/1464	2048/773	1435/226	886/112		
Octagonal CMA2 3.6b	1/512	1/1427	590/2048	1452/2048		10.9%
	2048/1520	2048/547	1530/1	537/1		

Table A.1.: Pixel positions of the two octagonal *EXOSAT* LE footprint shapes. The image has a size of 2048x2048 pixels.

ROSAT PSPC Pointed Encircled Energy Fraction (Zimmermann et al., 1998, eq.5.13)

$$r_1(E) = \frac{39.95}{E} \quad (\text{A.1})$$

$$r_2(E) = \frac{861.9}{E} \quad (\text{A.2})$$

$$R(E) = \sqrt{50.61E^{-1.472} + 6.8E^{5.62}} \quad (\text{A.3})$$

$$\alpha(E) = 2.119 + 0.212E \quad (\text{A.4})$$

$$\sigma(E, \epsilon) = \sqrt{108.7E^{-0.888} + 1.121E^6 + 0.219\epsilon^{2.848}} \quad (\text{A.5})$$

$$p_3(E) = 0.075E^{1.43} \quad (\text{A.6})$$

$$p_2(E, \epsilon) = \min \left\{ 10^{0.639E+0.052E^2-1.635} \cdot e^{-\left(\frac{\epsilon}{12}\right)^2/2}, 1 - p_3(E) \right\} \quad (\text{A.7})$$

$$p_1(E, \epsilon) = 1 - p_3(E) - p_2(E, \epsilon) \quad (\text{A.8})$$

$$M(E) = \frac{1}{\frac{1}{2} \ln \left[1 + \left(\frac{r_2}{r_1} \right)^2 \right] + \frac{1}{[\alpha(E)-2] \left[1 + \left(\frac{r_1}{r_2} \right)^2 \right]}} \quad (\text{A.9})$$

$$M(r, E) = M(E) \cdot \begin{cases} \frac{1}{2} \ln \left[1 + \left(\frac{r}{r_1(E)} \right)^2 \right], & r \leq r_2(E), \\ \frac{1}{2} \ln \left[1 + \left(\frac{r_2}{r_1} \right)^2 \right] + \frac{1 - \left(\frac{r}{r_2(E)} \right)^{\alpha(E)-2}}{[\alpha(E)-2] \left[1 + \left(\frac{r_1}{r_2} \right)^2 \right]}, & r > r_2(E) \end{cases} \quad (\text{A.10})$$

$$EEF(r, E, \epsilon) = p_1(E, \epsilon) \cdot \left[1 - e^{-\frac{1}{2} \left(\frac{r}{\sigma(E, \epsilon)} \right)^2} \right] + p_2(E, \epsilon) \cdot \left[1 - e^{-\frac{r}{R(E)}} \right] + p_3(E) \cdot M(r, E) \quad (\text{A.11})$$

Bibliography

- Arida, M. (1998).
ASCA Technical Description.
Technical Report.
https://heasarc.gsfc.nasa.gov/docs/asca/ao7/appendix_e/ao7_appendix_e.html.
Laboratory of High Energy Astrophysics, NASA GSFC, Greenbelt.
- Aschenbach, Bernd (1988).
“Design, construction, and performance of the ROSAT high-resolution x-ray mirror assembly”.
In: *Appl. Opt.* 27, pp. 1404–1413.
DOI: [10.1364/AO.27.001404](https://doi.org/10.1364/AO.27.001404).
- Bhardwaj, A. et al. (2007).
“X-rays from solar system objects”.
In: *Planet. Space Sci.* 55, pp. 1135–1189.
DOI: [10.1016/j.pss.2006.11.009](https://doi.org/10.1016/j.pss.2006.11.009).
- Bleeker, J. A. M. et al. (1967).
“Balloon Observation of the X-Ray Sources in the Cygnus Region in the Energy Range 20-130 KEV”.
In: *ApJ* 147, p. 391.
DOI: [10.1086/149019](https://doi.org/10.1086/149019).
- Boller, T. et al. (2016).
“Second ROSAT all-sky survey (2RXS) source catalogue”.
In: *A&A* 588, A103, A103.
DOI: [10.1051/0004-6361/201525648](https://doi.org/10.1051/0004-6361/201525648).
- Conner, J. P., W. D. Evans, and R. D. Belian (1969).
“The Recent Appearance of a New X-Ray Source in the Southern Sky”.
In: *ApJ* 157, p. L157.
DOI: [10.1086/180409](https://doi.org/10.1086/180409).
- Corliss, William R. (1971).
NASA SOUNDING ROCKETS, 1958-1968.
Historical report.
<https://history.nasa.gov/SP-4401.pdf>.
National Aeronautics and Space Administration.
- D.E. Harris, D. Irwin (1984).
Einstein Observatory Revised User's Manual.
Tech. rep. 2.
<https://heasarc.gsfc.nasa.gov/docs/einstein/>: Harvard-Smithsonian Center for Astrophysics.
- de Korte, P. A. J. et al. (1981).
“The X-ray imaging telescopes on EXOSAT”.
In: *Space Sci. Rev.* 30, pp. 495–511.
DOI: [10.1007/BF01246070](https://doi.org/10.1007/BF01246070).
- Dennerl, K. et al. (2002).
“Discovery of X-rays from Venus with Chandra”.
In: *A&A* 386, pp. 319–330.
DOI: [10.1051/0004-6361:20020097](https://doi.org/10.1051/0004-6361:20020097).
- Doschek, G. A. et al. (1980).

- “High-resolution X-ray spectra of solar flares. III - General spectral properties of X1-X5 type flares”.
 In: *ApJ* 239, pp. 725–737.
 DOI: [10.1086/158158](https://doi.org/10.1086/158158).
- Forman, W. et al. (1978).
 “The fourth Uhuru catalog of X-ray sources.”
 In: *ApJS* 38, pp. 357–412.
 DOI: [10.1086/190561](https://doi.org/10.1086/190561).
- Friedman, H., S. W. Lichtman, and E. T. Byram (1951).
 “Photon Counter Measurements of Solar X-Rays and Extreme Ultraviolet Light”.
 In: *Physical Review* 83, pp. 1025–1030.
 DOI: [10.1103/PhysRev.83.1025](https://doi.org/10.1103/PhysRev.83.1025).
- Gendreau, K. C. (1995).
 “X-Ray Ccds for Space Applications: Calibration, Radiation Hardness, and Use for Measuring the Spectrum of the Cosmic X-Ray Background”.
 PhD thesis. MASSACHUSETTS INSTITUTE OF TECHNOLOGY.
- Giacconi, R. et al. (1962).
 “Evidence for x Rays From Sources Outside the Solar System”.
 In: *Physical Review Letters* 9, pp. 439–443.
 DOI: [10.1103/PhysRevLett.9.439](https://doi.org/10.1103/PhysRevLett.9.439).
- Giacconi, R. et al. (1971).
 “An X-Ray Scan of the Galactic Plane from UHURU”.
 In: *ApJ* 165, p. L27.
 DOI: [10.1086/180711](https://doi.org/10.1086/180711).
- Giacconi, R. et al. (1979).
 “The Einstein /HEAO 2/ X-ray Observatory”.
 In: *ApJ* 230, pp. 540–550.
 DOI: [10.1086/157110](https://doi.org/10.1086/157110).
- Gioia, I. M. et al. (1990).
 “The Einstein Observatory Extended Medium-Sensitivity Survey. I - X-ray data and analysis”.
 In: *ApJS* 72, pp. 567–619.
 DOI: [10.1086/191426](https://doi.org/10.1086/191426).
- Gladstone, G. R. et al. (2002).
 “A pulsating auroral X-ray hot spot on Jupiter”.
 In: *Nature* 415, pp. 1000–1003.
 DOI: [10.1038/4151000a](https://doi.org/10.1038/4151000a).
- Gorenstein, P., F. R. Harnden Jr., and D. G. Fabricant (1981).
 “In orbit performance of the Einstein Observatory/HEAO-2 Imaging Proportional Counter”.
 In: *IEEE Transactions on Nuclear Science* 28, pp. 869–874.
 DOI: [10.1109/TNS.1981.4331295](https://doi.org/10.1109/TNS.1981.4331295).
- Gotthelf, E. V. and N. E. White (1997).
 “The ASCA SIS Source Catalog”.
 In: *X-Ray Imaging and Spectroscopy of Cosmic Hot Plasmas*.
 Ed. by F. Makino and K. Mitsuda,
 P. 31.
- Harnden Jr., F. R. et al. (1984).
 “Scientific Specification of the Data Analysis System for the EINSTEIN Observatory (HEAO-2) Imaging Proportional Counter”.
 In: *SAO Special Report* 393.
- Harris, D. E. (1990).
The Einstein Observatory Catalog of IPC X-ray Sources.
- Hayashida, K. et al. (1989).

- “The origin and behavior of the background in the large area counters on GINGA and its effect on the sensitivity”.
 In: *PASJ* 41, pp. 373–389.
- Jahoda, K., J. S. Allen, and L. A. Whitlock (1994).
 “HEAO-1 A2 Maps of the Hard X-ray Sky”.
 In: *American Astronomical Society Meeting Abstracts*.
 Vol. 26.
 Bulletin of the American Astronomical Society,
 P. 1429.
- King, A. R. and K. A. Pounds (2003).
 “Black hole winds”.
 In: *MNRAS* 345, pp. 657–659.
 DOI: [10.1046/j.1365-8711.2003.06980.x](https://doi.org/10.1046/j.1365-8711.2003.06980.x).
- Kormendy, J. and D. Richstone (1995).
 “Inward Bound—The Search For Supermassive Black Holes In Galactic Nuclei”.
 In: *ARA&A* 33, p. 581.
 DOI: [10.1146/annurev.aa.33.090195.003053](https://doi.org/10.1146/annurev.aa.33.090195.003053).
- Kraft, R. P., D. N. Burrows, and J. A. Nousek (1991).
 “Determination of confidence limits for experiments with low numbers of counts”.
 In: *ApJ* 374, pp. 344–355.
 DOI: [10.1086/170124](https://doi.org/10.1086/170124).
- Lisse, C. M. et al. (1996).
 “Discovery of X-ray and Extreme Ultraviolet Emission from Comet C/Hyakutake 1996 B2”.
 In: *Science* 274, pp. 205–209.
 DOI: [10.1126/science.274.5285.205](https://doi.org/10.1126/science.274.5285.205).
- Makino, F. and ASTRO-C Team (1987).
 “The X-ray astronomy satellite Astro-C”.
 In: *Astrophys. Lett.* 25, pp. 223–233.
- Mirabel, I. F. and L. F. Rodríguez (1994).
 “A superluminal source in the Galaxy”.
 In: *Nature* 371, pp. 46–48.
 DOI: [10.1038/371046a0](https://doi.org/10.1038/371046a0).
- Pfeffermann, E. et al. (1987).
 “The focal plane instrumentation of the ROSAT Telescope”.
 In: *Soft X-ray optics and technology*.
 Vol. 733.
 Society of Photo-Optical Instrumentation Engineers (SPIE) Conference Series,
 P. 519.
- Piccinotti, G. et al. (1982).
 “A complete X-ray sample of the high-latitude /absolute value of B greater than 20 deg/ sky from HEAO 1 A-2 - Log N-log S and luminosity functions”.
 In: *ApJ* 253, pp. 485–503.
 DOI: [10.1086/159651](https://doi.org/10.1086/159651).
- Pounds, K. (2002).
 “Forty years on from Aerobee 150: a personal perspective”.
 In: *Philosophical Transactions of the Royal Society of London Series A* 360, p. 1905.
 DOI: [10.1098/rsta.2002.1044](https://doi.org/10.1098/rsta.2002.1044).
- Pounds, K. A. et al. (1993).
 “The ROSAT Wide Field Camera all-sky survey of extreme-ultraviolet sources. I. The bright source catalogue.”
 In: *MNRAS* 260, pp. 77–102.
 DOI: [10.1093/mnras/260.1.77](https://doi.org/10.1093/mnras/260.1.77).

- Rothschild, R. et al. (1979).
 “The cosmic X-ray experiment aboard HEAO-1”.
 In: *Space Science Instrumentation* 4, pp. 269–301.
- Serlemitsos, P. J. et al. (1995).
 “The X-ray telescope on board ASCA”.
 In: *PASJ* 47, pp. 105–114.
- Stoehr, F. (2008).
 “Footprint Finder”.
 In: *Space Telescope European Coordinating Facility Newsletter* 45, p. 7.
- Troja, E. et al. (2017).
 “The X-ray counterpart to the gravitational-wave event GW170817”.
 In: *Nature* 551, pp. 71–74.
 DOI: [10.1038/nature24290](https://doi.org/10.1038/nature24290).
- Truemper, J. (1982).
 “The ROSAT mission”.
 In: *Advances in Space Research* 2, pp. 241–249.
 DOI: [10.1016/0273-1177\(82\)90070-9](https://doi.org/10.1016/0273-1177(82)90070-9).
- Truemper, J. et al. (1978).
 “Evidence for strong cyclotron line emission in the hard X-ray spectrum of Hercules X-1”.
 In: *ApJ* 219, pp. L105–L110.
 DOI: [10.1086/182617](https://doi.org/10.1086/182617).
- Tsusaka, Y. et al. (1995).
 “Characterization of the Advanced Satellite for Cosmology and Astrophysics x-ray telescope: preflight calibration and ray tracing”.
 In: *Appl. Opt.* 34, pp. 4848–4856.
 DOI: [10.1364/AO.34.004848](https://doi.org/10.1364/AO.34.004848).
- Turner, M. J. L., A. Smith, and H. U. Zimmermann (1981).
 “The medium energy instrument on EXOSAT”.
 In: *Space Sci. Rev.* 30, pp. 513–524.
 DOI: [10.1007/BF01246071](https://doi.org/10.1007/BF01246071).
- Turner, M. J. L. et al. (1989).
 “The large area counter on GINGA”.
 In: *PASJ* 41, pp. 345–372.
- Ueda, Y. et al. (2001).
 “The ASCA Medium Sensitivity Survey (the GIS Catalog Project): Source Catalog”.
 In: *ApJS* 133, pp. 1–52.
 DOI: [10.1086/319189](https://doi.org/10.1086/319189).
- (2005).
 “The ASCA Medium Sensitivity Survey (The GIS Catalog Project): Source Catalog II.”
 In: *ApJS* 161, pp. 185–223.
 DOI: [10.1086/468187](https://doi.org/10.1086/468187).
- Warwick, R. S. et al. (1981).
 “The Ariel V /3 A/ catalogue of X-ray sources. I - Sources at low galactic latitude /absolute value of B less than 10 deg/”.
 In: *MNRAS* 197, pp. 865–891.
 DOI: [10.1093/mnras/197.4.865](https://doi.org/10.1093/mnras/197.4.865).
- White, N. E. and A. Peacock (1988).
 “The EXOSAT Observatory”.
 In:
X-ray Astronomy with EXOSAT.
 Ed. by R. Pallavicini and N. E. White,
 P. 7.

Bibliography

Whitlock, L., J. Lochner, and K. Rhode (1992).

“The Ariel 5 and Vela 5B All-Sky Monitor Databases”.

In: *Legacy 2*.

Zimmermann, U. et al. (1998).

EXSAS User's Guide.

Tech. rep. 1.

ftp://ftp.xray.mpe.mpg.de/people/mjf/2RXS/exsas_guide-980708.pdf.

85740 Garching bei München, Germany: Max-Planck-Institut für Extraterrestrische Physik.